Spring 5-9-2017

CLASSIFICATION OF IMAGES BASED ON PIXELS THAT REPRESENT A SMALL PART OF THE SCENE. A CASE APPLIED TO MICROANEURYSMS IN FUNDUS RETINA IMAGES

Pablo F. Ordonez
Kennesaw State University

Pablo F. Ordonez

CLASSIFICATION OF IMAGES BASED ON PIXELS THAT REPRESENT A SMALL PART OF THE SCENE. A CASE APPLIED TO MICROANEURYSMS IN FUNDUS RETINA IMAGES

A Thesis Presented to
Department of Computer Science

By

Pablo F. Ordóñez

In Partial Fulfillment of the
Requirements for the Degree
Master of Science, Computer Science

KENNESAW STATE UNIVERSITY

May, 2017

CLASSIFICATION OF IMAGES BASED ON PIXELS THAT REPRESENT A SMALL PART OF THE SCENE. A CASE APPLIED TO MICROANEURYSMS IN FUNDUS RETINA IMAGES

Approved:

Dr. Jose Garrido - Advisor

Dr. Dan Chia-Tien Lo - Department Chair

Dr. Jon Preston - Dean

In presenting this thesis as a partial fulfillment of the requirements for an advanced degree from Kennesaw State University, I agree that the university library shall make it available for inspection and circulation in accordance with its regulations governing materials of this type. I agree that permission to copy from, or to publish, this thesis may be granted by the professor under whose direction it was written, or, in his absence, by the dean of the appropriate school when such copying or publication is solely for scholarly purposes and does not involve potential financial gain. It is understood that any copying from or publication of, this thesis which involves potential financial gain will not be allowed without written permission.

Pablo F. Ordóñez

Notice to

Borrowers

Unpublished theses deposited in the Library of Kennesaw State University must be used only in accordance with the stipulations prescribed by the author in the preceding statement.

The author of this thesis is:

Pablo F. Ordóñez

The director of this thesis is:

Dr. Jose Garrido

Users of this thesis not regularly enrolled as students at Kennesaw State University are required to attest acceptance of the preceding stipulations by signing below. Libraries borrowing this thesis for the use of their patrons are required to see that each user records here the information requested.

Name of user	Address	Date	Type of use (examination/copying)

CLASSIFICATION OF IMAGES BASED ON PIXELS THAT REPRESENT A SMALL PART OF THE SCENE. A CASE APPLIED TO MICROANEURYSMS IN FUNDUS RETINA IMAGES

An Abstract of
A Thesis Presented to
Department of Computer Science

By

Pablo F. Ordóñez
MSCS Student
Department of Computer Science
College of Computing and Software Engineering
Kennesaw State University, USA

In Partial Fulfillment of the
Requirements for the Degree
Master of Science, Computer Science

KENNESAW STATE UNIVERSITY

May, 2017

Abstract

Convolutional Neural Networks (CNNs), the state of the art in image classification, have proven to be as effective as an ophthalmologist, when detecting Referable Diabetic Retinopathy (RDR). Having a size of less than 1% of the total image, microaneurysms are early lesions in DR that are difficult to classify. The purpose of this thesis is to improve the accuracy of detection of microaneurysms using a model that includes two CNNs with different input image sizes, 60x60 and 420x420 pixels. These models were trained using the Kaggle and Messidor datasets and tested independently against the Kaggle dataset, showing a sensitivity of 95% and 91%, a specificity of 98% and 93%, and an area under the Receiver Operating Characteristics curve of 0.98 and 0.96, respectively, in the sliced images. Furthermore, by combining these trained models, there was a reduction of false positives for complete images by about 50% and a sensitivity of 96% when tested against the DIARETDB1 dataset . In addition, a powerful image pre-processing procedure was implemented, which included adjusting luminescence and color reduction, improving not only images for annotations, but also decreasing the number of epochs during training. Finally, a novel feedback operation that re-sent batches not classified as well as expected, increased the accuracy of the CNN 420 x 420 pixel input model.

CLASSIFICATION OF IMAGES BASED ON PIXELS THAT REPRESENT A SMALL PART OF THE SCENE. A CASE APPLIED TO MICROANEURYSMS IN FUNDUS RETINA IMAGES

A Thesis Presented to
Department of Computer Science

By

Pablo F. Ordóñez

Submitted in Partial Fulfillment of the
Requirements for the Degree
Master of Science, Computer Science

Advisor: Jose Garrido

KENNESAW STATE UNIVERSITY

May, 2017

This work is dedicated to the people that are dear to my heart. First I'd like to dedicate this to my father Pablo Emiro Ordóñez, in his memory. He taught me the value of knowledge and fasctination for undiscovered phenomenas. Secondly, my wife, Jacqueline Giraldo, whose unconditional love and support have alleviated my difficult moments and kept me pursuing my dreams. Finally, my daughter, Victoria Ordóñez, who is my inspiration and my greatest motive of happiness. Her sharp humor and acute critical sense of thinking enchant and brighten any of my dark days.

Utopia is on the horizon. I move two steps closer; it moves two steps further away. I walk another ten steps and the horizon runs ten steps further away. As much as I may walk, I'll never reach it. So what's the point of utopia? The point is this: to keep walking.

Eduardo Galeano

ACKNOWLEDGEMENTS

I would like to thank Dr. Jose Garrido who rescued and valued our work. His door was always open to listen to my problems and to provide me with wise advice. My appreciation for you is in my mind and soul forever.

I would also like to thank Dr. Sumit Chakravarty. His contributions and feedback to this project were invaluable and his extensive knowledge in the field was fundamental to find the right direction for which this study was headed. In addition, his dedication to this work exceeded any student imagination, and his willingness to improve our work encouraged me to give it my best effort.

I want to give a special thanks to Dr. Dan Lo, who facilitated and mediated the final phase of this work.

Also, I would like to express my gratitude to my friend and "brother", Carlos Cepeda, who seeded the love for math in my brain. We spent long nights decoding the complexity of this science and were vigilant of each other researches.

I want to thanks to Dr Chih-Cheng Hung who taught me the alphabet of image processing and let me be a part of his lab for some time.

I would like to express my deep appreciation for the Dabney family (Joseph, Susanne, Earl, Geneva, Scott, Mark, Chris), who embrace me as their own family member and were practically my second family.

Finally, I want to express my very profound gratitude and respect to my family in Colombia, my mother Mery and my brother Wilson Renier who nurtured me in my early years.

List of Tables

List of Figures

TABLE OF CONTENTS

CHAPTER 1

INTRODUCTION

The development of a non-invasive method that detects Diabetes during its early stages would improve the prognosis of patients. The prevalence of Diabetes in the US is approximately 9.3%, affecting 29.1 million people [1]. The retina is targeted in the early stages of Diabetes, and the prevalence of Diabetic Retinophaty (DR) increases with the duration of the disease. Microaneurysms are early lesions of the retina, and as the disease progresses, damage to the retina includes exudates, hemorrhages, and vessel proliferation. The detection of DR in its early stages can prevent serious complications, like retinal detachment, Glaucoma and blindness. The screening methods used to detect Diabetes are invasive test, the most popular one being measuring blood sugar levels. Fundus Image Analysis is a non-invasive method that allows healthcare providers to identify DR in its early stage; a procedure now performed in clinical settings. The massification of devices that help cell phone cameras take the fundus image would make this procedure available for all populations [1]. Once the image is obtained, it can be loaded to a cloud service and analyzed to detect microaneurysms.

The clinical classification of DR reflects its severity. A consensus in 2003 [2] proposed the Diabetic Retinopathy Disease Severity Scale, which consists of five classes for DR. Class zero or the normal class has no abnormalities in the retina; class one, or the mild class, shows only less than five mycroaneurysms; class two or the moderate class is considered as the intermediate state between class one and three; class three or the severe class contains either more than 20 intrarretinal hemorrhages in one of the four quadrants, venous beading

[1] https://www.welchallyn.com/en/microsites/iexaminer.html

in two quadrants, or intrarretinal microvascular abnormalities in one quadrant; class four or the proliferative class includes neovascularization, or vitreous and preretinal hemorrhages. The severity level of the disease progresses from class one to four and special consideration is given to lesions close to the macular area.

Machine learning (ML) is evolving constantly and embracing other fields of science. ML emerged from the intersection of several fields such as artificial intelligence, statistics, and computational learning theory. The aim of ML is to develop algorithms that can discover patterns from complex data and use those patterns to make predictions on new data. One of those algorithms is Neural Networks (NNs) which evolved to Deep Neural Networks (DNNs). The idea behind DNNs is not only to increase the number of layers, but also to learn hierarchical representations in each layer. In computer vision, a specialized form of DNNs, Convolutional Neural Networks (CNNs), debuted on the nineties, which incorporated convolutional layers in its architecture.

The Convolutional Neural Network (CNN) is the most effective method of classification for images. CNNs are state of the art image classifications based on Image-net [2] and COCO 2016 Detection [3] challenges. Since CNN's initial design, [3] not only its architecture [4, 5, 6, 7], but also its regularization parameters, weight initialization [8, 9], and neural activation function [10] have evolved. Within medical image analysis, CNN has been applied in several areas like breast and lung cancer detection [11, 12]. Specifically in fundus retina images, CNN has proven to be the best automatized system when detecting Referable Diabetic Retinopathy [13], moderate and severe, surpassing other algorithms performing the same task [14].

Classification of images based on small objects is difficult. Although CNN classifies moderate and severe stages of DR very well, when classifying lesions that belong to class

[2] http://image-net.org/challenges/LSVRC/2016/results
[3] http://mscoco.org/dataset/#detections-leaderboard

one and two, it has some flaws. The lesions in these classes contain microaneurysms with a maximum size of less than 1% of the entire image. For instance, Pratt's study [15] shows a total accuracy of 75%. However, from the 372 patients in class one, none were classified correctly; 92% were classified as normal, and the rest were divided between class two and four. Gilbert's work [16] proved that when detecting microaneurysms, the proportion of false positives per image is close to 90% when they try to reach a sensitivity of 90%. In the same study, the detection of exudates was better performed than the detection of microanuerysms. The purpose of this study is to improve the accuracy of detection of microaneurysms.

CHAPTER 2

RELATED WORK AND PROBLEM DEFINITION

2.1 Related Work Overview

Medical Imaging is one of Machine Learning's prolific fields. CNN has been used in medical diagnosis since 1996 [17] to differentiate malignant masses from normal masses in mammograms. CNN has expanded its utility from detection to segmentation [18] and shape modeling [19]. Because the focus of this study is the detection of early lesions in DR, this chapter will discuss the recent studies addressing this problem based on the authors' interest to classify some or all of the lesions.

2.1.1

hspace1emDetecting All Stages

Pratt's study [15] shows the difficulty of detecting lesions in stage one. In this study, the Kaggle dataset was used to classify all of DR's categories. The input size was obtained by resizing the images from their original size to a size of 512×512 pixels. Pratt's CNN design included ten convolution layers, three full connected layers, the maxpooling function, the ReLu activation function, and Batch Normalization. The study had a global sensitivity of 95% and an accuracy of 75%. However, as shown in Table 2.1, it preformed poorly when classifying mild lesions since none of the microaneurysms were classified correctly.

Table 2.1: PRATT'S CONFUSION MATRIX

		Predicted Level				
		Normal	Mild	Moderate	Severe	Proliferative
True Label	Normal	3456	0	145	1	34
	Mild	344	0	27	0	1
	Moderate	543	0	179	5	40
	Severe	40	0	63	10	15
	Proliferative	28	0	23	3	43

2.1.2

hspace1emDetecting Advanced Stages

Gulshan's study [13] proved the CNN's efficacy of detecting moderate and severe stages of DR. In this study, CNN Training was done using the Kaggle dataset. The goal of this study was to measure the sensitivity and specificity of the CNN to detect Referable DR. The author used Inceptionv3 architecture for training, and the training weights of the CNN were tested against the Kaggle and Messidor sets. Table 2.2 shows that the algorithms performed well when detecting moderate, severe, and macular edema in the images. Although this model had a sensitivity of 90%, its AUC of 99% was comparable to that of an Ophthalmologist.

Table 2.2: ALGORITHM PERFORMANCE

	Kaggle		Messidor	
	Sensitivity	Specificity	Sensitivity	Specificity
Moderate	90.1	98.2	86.6	98.4
Severe	84	98.9	87.8	98.2
Macular Edema	90.8	98.7	90.4	98.8

2.1.3

hspace1emDetecting Early Stages

Gilbert [16] was the first author to use the CNN to classify individual lesions. His work used an automatized algorithm, Multiscale C-MSER Segmentation, to crop the region of interest (ROI) with the lesion in the center of the image. DIARETDB1 and SiDRP datasets were chosen for training and testing. Gilbert's CNN design had four convolution layers, two full connected layers, and images with an input size of 47 $\times$ 47 pixels. Fig 2.1 shows the results of microaneurysm detection in the mentioned datasets. Gilbert reached a sensitivity of 30% with a specificity of 100%, but increasing the sensitivity increased the number of false positives per image as shown in Fig 2.1a. Testing the trained CNN with the SiDRP dataset performed better than testing the CNN with DIARETDB1 as shown in the Fig. 2.1b.

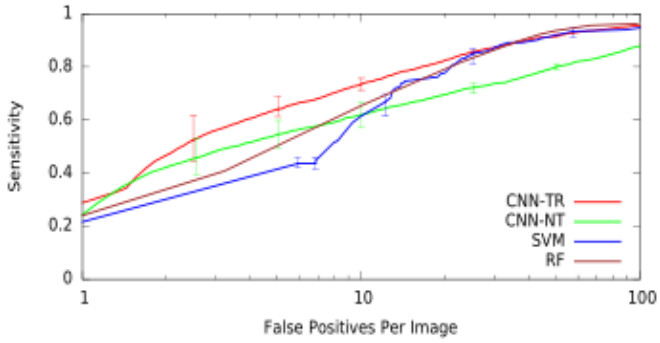

(a) Microaneurysms SiDRP

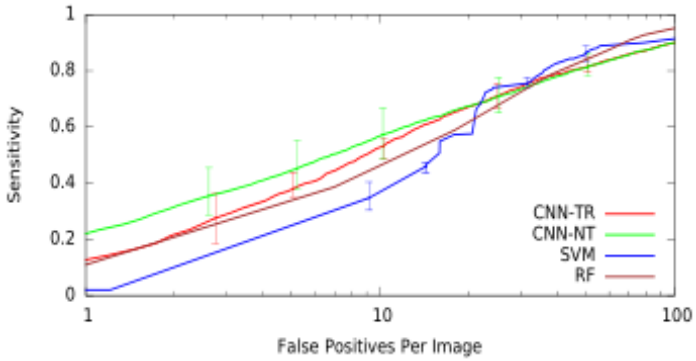

(b) Microaneurysms DIARETDB1

Figure 2.1: Microaneurysms Detection

Grinsven's study [20] focused on hemorrhage detection.The Kaggle dataset was used for training and the Kaggle and Messidor datasets were used for testing. Hemorrhages were selected from the experts' annotations, followed by the cropping of images with the lesion in the center. The input size of the images was 41 $\times$ 41 pixels, and the CNN's design contained five convolution layers and one full connected layer. Another feature of this study was the implementation of selective data sampling, a methodology that mimics a feedback mechanism for normal class images. At the beginning of the training, all of the normal images had an assigned score probability. This score determined the chance the image had of being selected in the next batch. During training, normal images that were classified incorrectly would increase their score probability, so they would have a higher chance of being trained in the next batch. The author used the area under the curve of the ROC to measure the CNN's performance. The trained CNN had a 0.894 AUC tested against the Kaggle dataset as shown in Fig. 2.2a and 0.972 AUC tested against the Messidor dataset as depicted in Fig. 2.2b. One of the disadvantages of this approach was that the lesion was in the center of the image. This lead to the CNN learning the position of the lesion instead of its intrinsic features. Another disadvantage was the high number of false positives in the testing despite the implemented feedback mechanism. Finally, the last drawback was that this methodology used a lot of computing power in the testing.

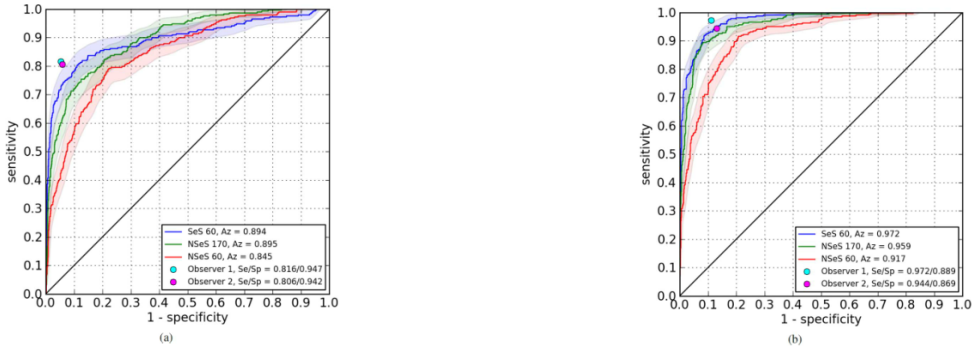

(a) ROC Kaggle Hemorrhage Detection

(b) ROC Messidor Hemorrhage Detection

Figure 2.2: ROC Hemorrhage Detection

2.2 Problem Definition And Proposed Solution

Microaneurysm detection in DR is a complex challenge. As mentioned in the previous section, the difficulty of this task is determined mainly by the size of the lesions. The last two studies tried to overcome this obstacle by cropping the image with the lesion in the center without changing the resolution. Although these studies have an acceptable sensitivity and specificity, the number of false positives is considerable. The following example will explain the reason of having a high number of false positives: Having an image size of 2000 $\times$ 2000 pixels will generate 2304 images with a size of 41 $\times$ 41 pixels, so having a specificity of 90% will produce 231 false positive images with a size of 41 $\times$ 41. Another important aspect in microaneurysm detection in DR is the quality of the image. Although it is not mentioned in the review, some algorithms performed better when they were tested with the Messidor dataset instead of the Kaggle dataset. It is known that the Messidor dataset is a small dataset that has high quality images, while the Kaggle dataset is the most important dataset, due to the size, with an acceptable quality. We hypothesized that a good image pre-processing method would surpass this difficulty.

The aim of this study was to detect microhemorrhages of DR using Convolutional Neural Networks. We hypothesized that using two tests, one with high sensitivity and the other with high specificity, would decrease the false positive rate. One test is a CNN trained with an image that has a small size of 60 $\times$ 60 pixels, and the second test is a CNN trained with an image that has a size of 420 $\times$ 420 pixels. While the first test will find all the lesions in the images; the second test will better distinguish the difference between normal and abnormal images.

During the study, other parameters would be measured such as the impact of augmentation versus new input in accuracy and the use of a feedback mechanism.

CHAPTER 3

CNN REVISION

3.1 Introduction

Common tasks like asking your phone for directions, asking an electronic device to turn on the AC, or asking your computer to read aloud a document is possible due to advances in Machine Learning algorithms. The algorithms recognizing different patterns from the input data [21] allow those devices to perform those tasks. One such algorithm is Artificial Neural Networks (ANNs), which consists of layers of interconnected nodes (neurons). The connections between these nodes have a dynamic value (weight) and each node performs a summative function of their coming weights. Finally, a threshold function of the sum of the weights determines the signal propagation of the nodes for the next layer. This design tries to mimic the neuron connections in humans where inhibitory and excitatory neurotransmitters will stop or propagate an electrical impulse [22, 23, 24]. In addition, learning functions [25] were developed to modify the weights dynamically, making the system autonomous and self-learning. Fig. 3.1 shows a diagram of an ANN formed by three layers: the first layer being the input layer, the second being the hidden layer, and the third being the output layer.

The idea of Deep Learning (DL) not only implies an increase in the number of layers in the ANN, but also the concept of learning multiple levels of representation in each layer [27, 25, 7]. The ANN evolved over time and more layers have been added to the original design, improving the results in different tasks. Fig 3.2 shows the difference between classical ML

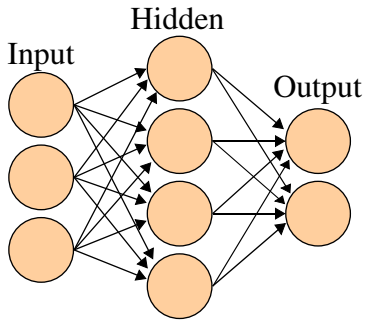

Figure 3.1: Diagram ANN[26]

and Representation Learning; DL builds abstract features in deep layers based on simple features in the initial layers. Independent of the number of the layers, the representation-level of each layer is different. For example, in a CNN the first layer learns features to detect specific edges of the images. The second layer's weights detect mofits by combining some of the edges. The third layer learns to detect partial objects by the combination of mofits. The learned features in the fourth layer detects objects by associating parts of the previous layers.

One specific design of DL from Fukushima [28] influenced Yan Lecun to develop the concept of Convolutional Neural Networks (CNN) [29, 3]. CNNs are specialized ANNs that perform convolution operations instead of full matrix multiplication. In the 90's and early 2000's, the algorithm under-performed compared to other algorithms of ML for the same task. However, with the advances in power computing, the availability of big data, the flexibility of the models, and the modifications in the algorithm that defeat the curse of dimentionality, Deep Learning has become a leading methodology. Nowadays, the CNN has became the state of the art in classification, object recognition and segmentation. The CNN aggregates an input layer followed by multiple sequential modules and finishes with a classical ANN. Each module consists of convolution, max pooling, and activation function stages. The output of each module are the weights of the next module.

Supervised learning is the most common form of training for ML. Having labels for the

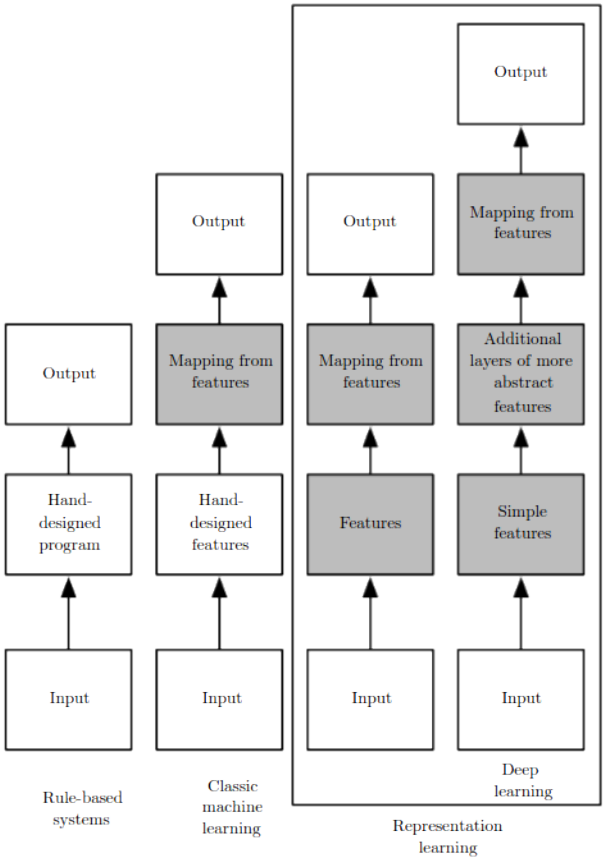

Figure 3.2: Feature Discovering [27]

input allows the algorithm to compare the forward results of the CNN to the input labels using a Cost Function. This function determines the distance (error) from the result of the ANN and the image labels. Then the system adjusts the weights of the model using learning algorithms like the stochastic gradient descendant (SGD). The weights in each layer are adjusted using backpropagation before repeating a new cycle. The number of cycles is not a constant and most researchers stop the training when overfitting is present, which can be analyzed by looking at the accuracy curve for the training and validation sets.

3.2 Input And Output

Our input includes two dimensional (2D) arrays containing the intensity values between 0 to 255 for each channel (RGB). For example, in an image with a size of 420 $\times$ 420 pixels, the input is a three dimensional matrix (3D) of 420 $\times$ 420 $\times$ 3 pixels. The output is the probability of the image belonging to a certain class.

3.3 Convolution

Convolution is a mathematical operation defined in the discrete form of two dimensional images as follows:

$$s[i,] = (I * K)[i,j] = \sum_m \sum_n I[m,n]K[i-m, j-n]\,, \tag{3.1}$$

where x is the input, w is the kernel, and the output known as *Feature Map*. Convolutions have three inherent characteristics to improve the ML algorithm: *sparce interactions, parameter sharing*, and *equivalent representation*.

Sparce Interactions refers to the fact that using kernels with a size less than the input size reduces the number of parameters. If we have an input with a size of 100 $\times$ 100 pixels that it is fully connected to 10 hidden neurons, then we will have 100000 parameters plus 10 bias parameters. On the other side, a convolution with a kernel size of $3 \times 3 \times 20$ has 180 parameters. Reduction in the number of parameters would diminish the computing power needed to train the CNN. Another side effect of sparce interactions, is the pyramidal structure of the *receptive field* which means deeper layers are influenced indirectly by the upper layers as shown in Fig. 3.3

Parameter Sharing describes the use of the same parameters (the weights of the kernels)

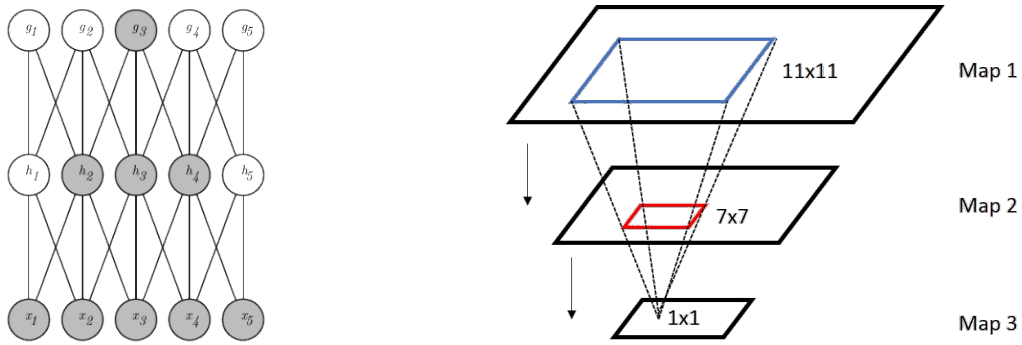

(a) Neurons View [27] (b) Feature Map View

Figure 3.3: The Receptive Field

to perform the convolution operation in the whole image. A side effect of this convolution feature is that learning is performed on each set of kernels and not on individual weights. On the left side, Fig 3.4 shows dark lines that are the central parameters of a 3 element kernel connected layer. Here, a single parameter is used for all of the inputs. The right side of the Fig 3.4 depicts a standard ANN where all of the parameters are used once [30].

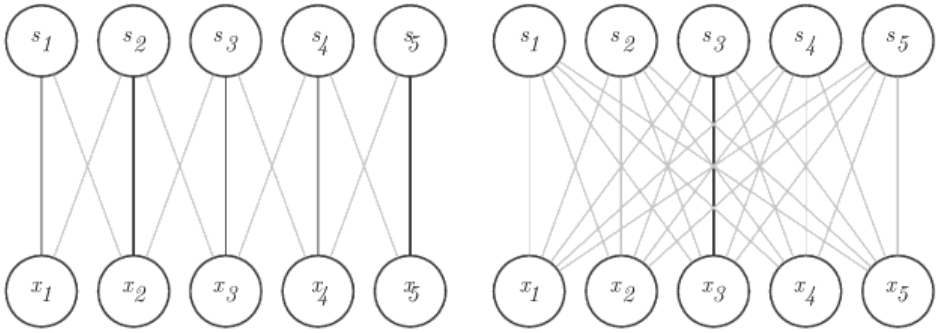

Figure 3.4: Parameter Sharing [27]

Equivalent Representation alludes to the fact that changing the order within the convolution and any function would not alter the final result. In other words, changing the order of the layers in the module will produce the same Feature Maps.

3.4 Pooling

Pooling is a function that downsamples the size of the input. Fig 3.5 displays a Max Pooling function with a filter of 2×2 pixels and a stride of 2 pixels. The maximum value of the filter is kept and the filter moves 2 positions to the left. The goals of pooling are to reduce the number of parameters, computational work, and to produce a feature map with less invariance to the translation. Several pooling functions are available, such as fractional max pooling or average pooling.

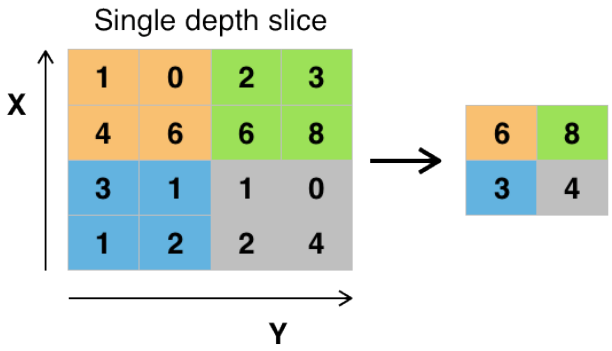

Figure 3.5: Max Pooling [31]

3.5 Neural Network Architectures

The initial design by Lecun [3] in 1988 has evolved rapidly within the last few years. LeNet5 [32] has 2 modules, and each of these have a sequence of convolution, subsampling, and a non-linear activation function layer. A Multi-Layer Perceptron (MLP) containing 3 full connected layers and the output layer is the last part of the design. Fig 3.6 shows Lenet5's model.

In 2012, AlexNet's architecture [33] made a big jump from Lenet5 architecture. The design was deeper and they used Maxpooling and ReLu. In addition, AlexNet was trained with GPUs which made the process faster. Fig. 3.7 displays Alex Krizhevsky' design.

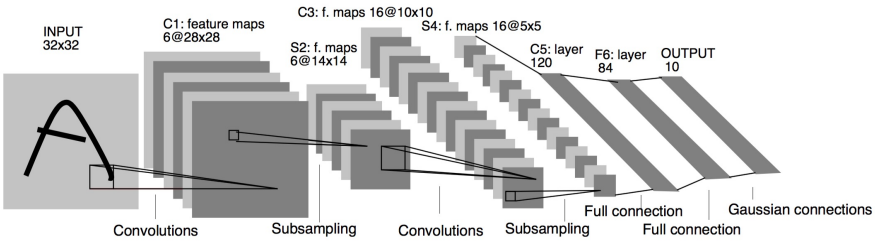

Figure 3.6: Lenet5 [31]

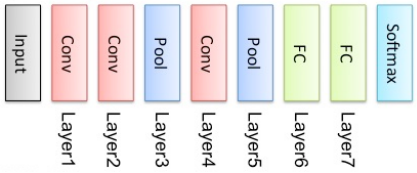

Figure 3.7: AlexNet

Simoyan developed VGG architecture [5]. The design used small filters for convolutions and repeated the convolution layer in each module. Fig 3.8 shows one type of VGG architecture. However, other designs would have 3-4 convolutional layers for each module.

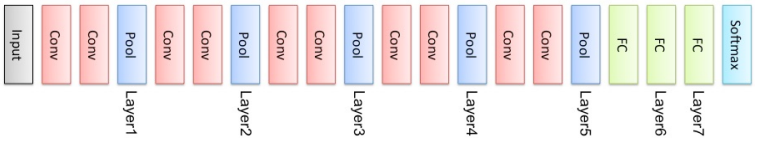

Figure 3.8: VGG

Christian Szegedy [7] came up with the idea to not only make the CNN deeper but to also make it wider for each module. Each module is considered a network within the network and the output size of the module could be the same size of the input. Later, modifications of the original design helped develop Inceptionv2 [9, 34] and Inceptionv3 [35]. Fig 3.9 depicts the composition of the module in Inceptionv1 and Inceptionv3. Fig 3.10 displays the full architecture of Inceptionv3. One common feature of these types of deep architectures is that the deeper the design, the wider each module becomes.

Microsoft's group developed ResNet [36], whose design was characterized by feeding the output to two sequential convolution layers and bypassing the input to the next layers.

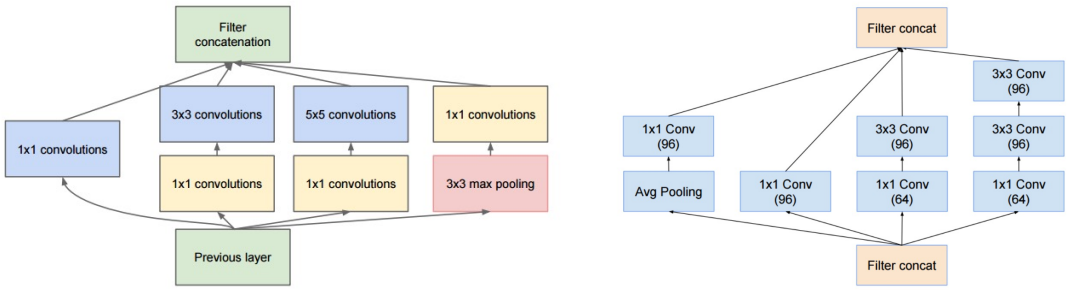

(a) Inceptionv1 (b) Inceptionv3

Figure 3.9: Inception

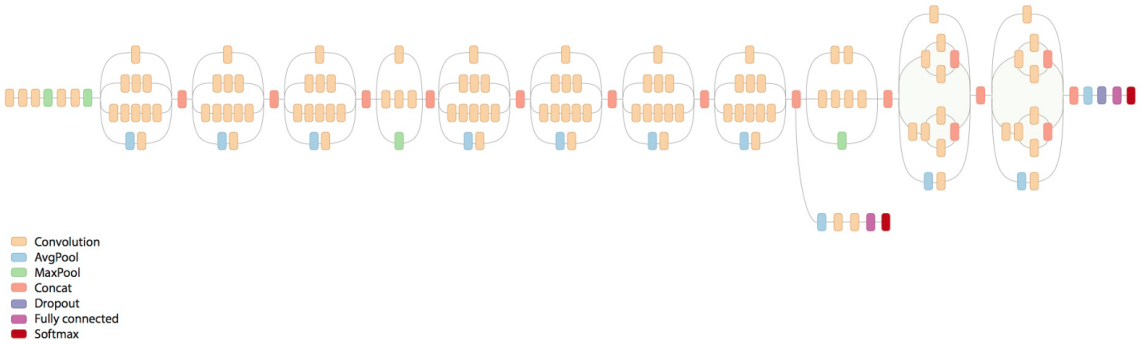

Figure 3.10: Inception V4

Fig. 3.11b shows a RetNet design with 34 layers and Fig. 3.11a displays a module with 3 sequential convolutions and input feed.

3.6 Other Definitions

3.6.1

hspace1emDropout

Dropout is the process in which some neurons in the forward pass are excluded from the training [37]. The benefit of dropout is the avoidance of overfitting. It is important that

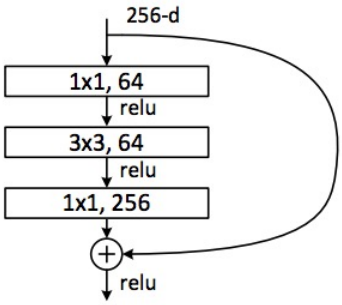

(a) Feed Input

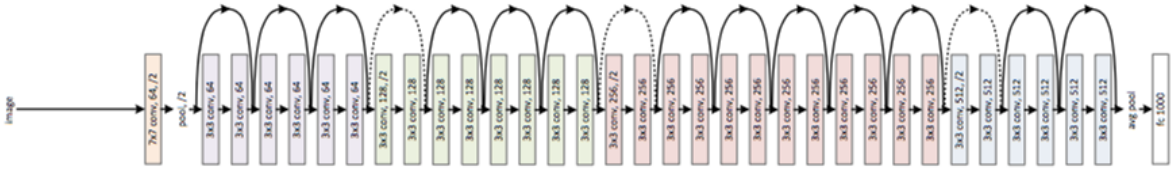

(b) RetNet 34 Layers

Figure 3.11: RetNet

all the weights be present during testing phase. Some studies support this approach while others have obtained little benefit from this. However, dropout has become a standard in most of the models.

3.6.2 hspace1emAugmentation

Due to the small number of samples in the datasets, researchers came up with a procedure called augmentation to defeat this contingency. Augmentation is an artificial manner to expand the data. Several operations are available to perform augmentation like translation, rotation, warping, horizontal or vertical flipping, cropping and jittering.

3.6.3

hspace1emReLu

ReLu is an activation function, that according to some studies, would prevent the vanishing gradient problem. The ReLu function, $f(x) = max(0, x)$, is applied to the end of each module, generally after pooling. The Leaked Rectifier Units (LeReLu) function is a modification of the ReLu function in which the number 0 in $max(0, x)$ is replaced by any negative value.

3.6.4

hspace1emStride And Padding

Stride is the number of pixels that a filter should jump to perform the next operation, usually within a convolution or pooling function. Fig. 3.12a shows a convolution kernel moving with a stride 2. After applying a convolution function, the borders of the input are excluded, but adding zeros to those pixels helps keep a desired size. This operation is called padding. Fig. 3.12b illustrates a padding of zeros to increase the size of the input from 32×32 to 36×36 pixels.

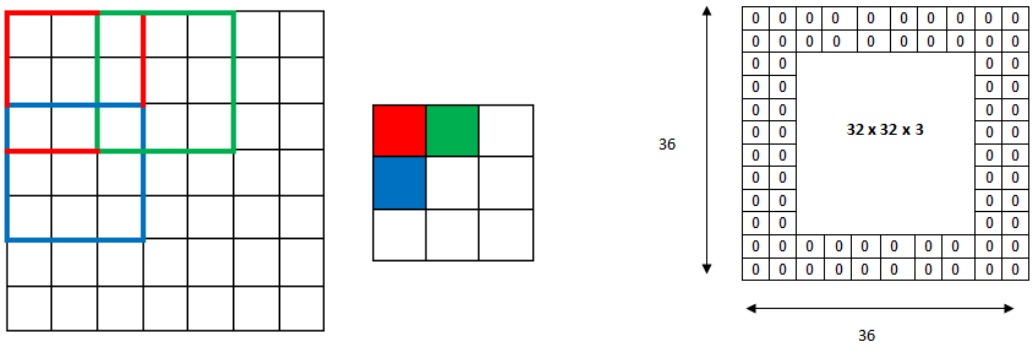

(a) Stride 2 [31] (b) Padding [31]

Figure 3.12: Stride and Padding

CHAPTER 4

RESOURCES

4.1 Databases

The data sets utilized in this study are Kaggle diabetic-retinopathy-detection competition [1], Messidor datatabase [2], and the Diabetic Retinopathy Database and Evaluation Protocol [3].

4.1.1

hspace1emDataset Features

The majority of the available databases contain DR images of all classes. However, because the aim of our study is to detect microaneurysms, and to differentiate images with and without lesions, we chose images that only belong to class zero, one, and two (Messidor).

i. Kaggle Dataset: Eyepacs provided the images to Kaggle, where we accessed them and used them in our study. This dataset implements the Clinical Diabetic Retinopathy Scale to determine the severity of DR (none, mild, moderate, severe, proliferative) and contains 88702 fundus images. Table 4.1 shows unbalanced data with prominent differences between mild and normal classes. It is also evident that most of the images belong to the testing set.

[1] https://www.kaggle.com/diabetic-retinopathy-detection
[2] Kindly provided by the Messidor program partners (see http://www.adcis.net/en/DownloadThirdParty/Messidor.html)
[3] http://www.it.lut.fi/project/imageret

Table 4.1: KAGGLE RAW DATABASE

	Training	Testing
All	35126	53576
Normal	25810	39533
Mild	2443	3762

The subset for our study includes 21203 images, in which 9441 are used for training, and 11672 are used for testing. We selected random samples from the *normal* class, that have at most a confidence interval of 1, a confidence level of 95%, and selected all of the cases in the *mild* class. The testing set was subdivided into a validation and testing set.

Table 4.2: STUDY DATABASE

	Kaggle		Messidor	DiaRetDB1
	Training	Testing	Training	Testing
Normal	8000	8000		
Class 1	2443	3762	153	
Class 2			246	
All				89

ii. Messidor Dataset: Within the public domain, 1200 eye fundus color images of all classes are provided by the Messidor dataset. The annotation includes a retinophaty grade of (0-3) and a risk of macular edema grade of (0-2), where grades one and two were included in the training set. From those, 153 are classified as grade one and 246 as grade two, where isolated microaneurysms were only selected. From the author's perspective, Messidor images are of excellent quality and have very few artifacts.

iii. Diabetic Retinopathy Database and Evaluation Protocol (DIARETDB1) is a public set of 89 images with a standard dimension of 1500 $\times$ 1152 pixels. This dataset

also includes ground truth annotations of the lesions from four experts, which are labeled as small red dots, hemorrhage, hard exudates, and soft exudates. We parsed the xml files with the annotations, to get the coordinates of the small red dots and hemorrhages. This set will be used for testing purposes.

Table 4.2 shows the number of images per class in each database used in the study.

4.2 Image Annotations

The main author of this study, a medical doctor and General Surgeon, was the person who located and annotated the microaneurysms in the images that belong to class one and two. The range of difficulty to localize these lesions varies, but for the purpose of this study the authors chose only the evident lesions from these images, leaving dubious images out of the study. Some pictures have more than one microaneurysm and each is counted as different in this study.

4.3 Machine Learning Framework

Torch [4] was the framework chosen for this study and the multi-gpu Lua scripts [5] were adapted to run the experiments. Other frameworks used in this study include OpenCV for imaging processing, R-Cran for statistical analysis and plotting and Gnuplot for plotting. The training of the CNNs was performed on a 16.04 Ubutu Server with four Nividia M40 GPU's using Cuda 8.0, and Cudnn 8.0.

[4] http://torch.ch/

[5] https://github.com/soumith/imagenet-multiGPU.torch

CHAPTER 5

METHODS USED TO IMPLEMENT OUR PROPOSED SOLUTION

An improved image was created for the annotations by applying an original pre-processing approach. Once the author selected the coordinates of the lesions, the cropping of the images with the lesions and the cropping of normal fundus images was executed. Two datasets with cropped sizes of 60x60 and 420x420 were obtained and trained using modified CNNs. One of our modifications included a novel feedback mechanism for training. We also evaluated the increase in the size of the dataset by using either augmentation or adding new images. Receiver Operating Characteristics (ROC) [38] was used to get the cut-off of the predicted values in order to obtain a more accurate sensitivity and specificity of the models. Lastly, an analysis on the more precise model with the DiaRetDB1 was performed to find its overall sensitivity.

5.1 Processing Images

Batch transformations on the lightness and color of the images were used to produce higher quality images for annotations and a comparative analysis of using CNNs with inputs of images with and without pre-processing was performed.

Initially, the images were trimmed to eliminate the black border, which did not add any value; on the contrary, it only added noise to the study's purpose. Then, the descriptive statistics were calculated and K-means analysis was used to divide the images in three groups (dark, normal, and bright). A function based on the statistics was performed to

transform the lightness of the images using LAB color space. After collecting the a^* and b^* intensity values in the LAB color space from vessels, microaneurysms, hemorrhages, and a normal background, a Support Vector Machine (SVM) was used to separate microaneurysms and hemorrhages from the background. Based on the SVM, another function used to reduce the color of the image based on the LAB color space was created.

5.1.1

hspace1emGetting Images Statistics

LAB color space was chosen due to its property of separating luminescence from color. All of the images from the training sets were converted to LAB color space. After that, the mean and standard deviation for each image was obtained and their statics were derived. Table 5.1 shows the descriptive statistics of all of the images in the training sets and Fig. 5.1 displays each image with the mean represented by the $y - axis$ and the standard deviation represented by the $x - axis$. The range values in Table 5.1 and the box-plots in Fig. 5.1 shows some variety within the training set images. For the purpose of this study, we used the mean nd standard deviation of the images to normalize, cluster, and develop a method for lightness adjustment.

Table 5.1: TRAIN IMAGES STATISTICS

		Mean	Std	Min	Max	Range
Mean Per Picture	L*	33.93	11.83	0.70	80.22	79.52
	a*	11.07	7.35	-9.01	47.63	56.63
	b*	18.23	8.63	-2.11	59.82	61.93
Std Per Picture	L*	18.09	4.83	0.42	37.38	36.95
	a*	8.32	3.24	0.21	21.67	21.45
	b*	10.97	3.76	0.42	24.54	24.12

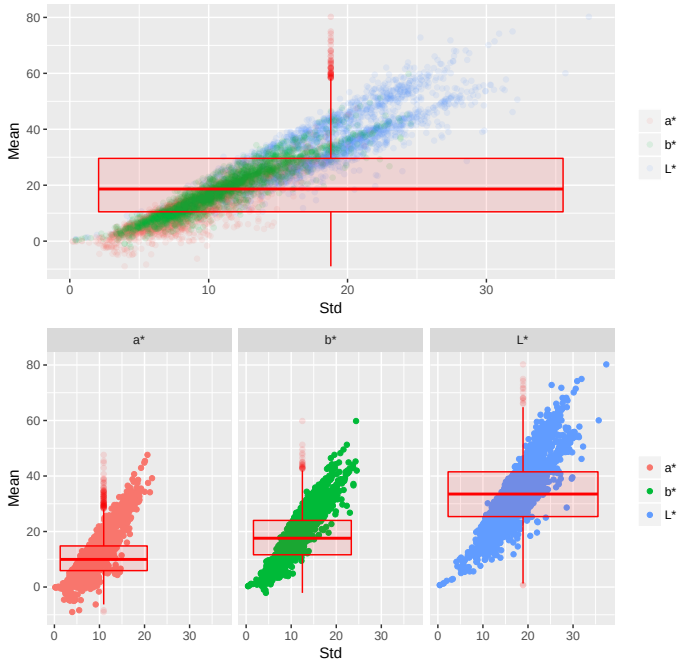

Figure 5.1: $L^*,\ a^*,\ b^*$ channels distribution

5.1.2

hspace1emNormalization

Unlike the data normalization used in CNN training, the goal of the pre-processing normalization was to not center the data around zero. In addition, the normalization should and was done to each pixel with respect to its own image, to all of the images, and to each one of their channels ($L^*,\ a^*,\ b^*$). Finally, the result was displayed using a standard software package, which in our case was OpenCV. Our image normalization Equation was

$$npv = (pv - mp) \times \frac{stdap}{stdp} \times k_1 + map + k_2\,, \tag{5.1}$$

where pv is the pixel value, npv the new pixel value, mp the mean value of the images, map the mean value of all the imagess, $stdp$ the standard deviation value of the imagess, and $stdap$ the standard deviation value of all the imagess. The first part of the equation normalizes the pixel value based on the mean of the images and adjusts its value according

to the proportion of the standard deviation of all the imagess and the images that owns the pixel value. The second part of the equation re-positions the pixel value based on the mean of all the imagess. Fig. 5.2 shows the steps for normalization, where the continuous line represents the density probability of all the imagess, the discontinuous line represents the density probability of one images, and the histogram represents the distribution of the pixels values in one images.

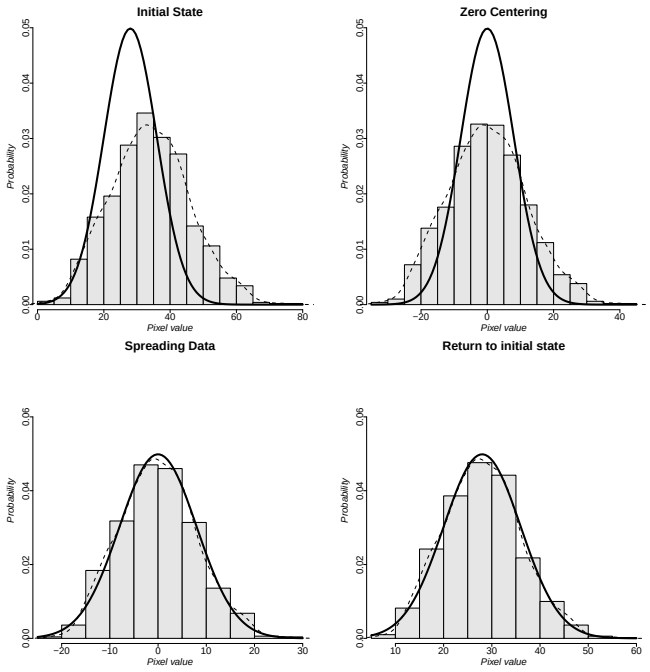

Figure 5.2: Pixel Normalization

5.1.3

hspace1emAdjust Luminance Intensity for a Batch

From a simple visual inspection of the random images, dark, normal, and clear images can be found, which ratify the wide range in the L* channel being displayed in Table 5.1. A method used to modify the brightness of all the images in a batch is described next.

Lab color space represents color-opponent dimensions in Fig 5.3. The lightness is given

by the **L*** channel and the values indicate the position of the light-dark axis, with zero being the darkest black and a hundred being the brightest white. The **a*** values indicate the position of the red/green axis within a range of -128(green) to 127 (red), and the **b*** values indicate the position of the blue/yellow axis within a range of -128(blue) to 128 (yellow)[39].

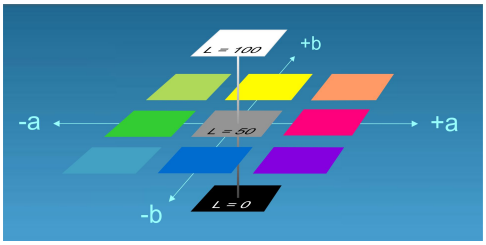

Figure 5.3: CIE Lab Color Space.[40]

Once the images were normalized, an analysis of the distribution of the mean and standard deviation of the lightness of each image in the training sets was done. The elbow method was used [41] to obtain the optimal number of clusters from this data. Fig 5.4a (top) shows 5 as the optimal number of clusters, and the mean and standard deviation values of those centroids are displayed in Table 5.2. Fig 5.4a (bottom) also displayed the cluster data with its centroids.

Table 5.2: CENTROIDS L* CHANNEL

Centroid	Mean	Std
1	14.67	10.26
2	24.40	14.66
3	33.20	18.21
4	41.81	21.14
5	54.17	24.86

Fig. 5.4a (bottom) reveals that most of the cases are between clusters two and four and Fig 5.4b shows that clusters one and five represent the darkest and brightest images respectively. The mean pixel value of the 25th percentile of the first clusters is ten, which

was set as the lower limit for the transformation. We visually inspected the images with a mean value of the L^* channel lower than ten and found that the images were too dark to be readable. Notice that there are not any images with values in the y axis above 80, making this value our superior limit for the transformation. A sample of some of the images from other clusters was evaluated and we noticed that high quality images belong to the third cluster. With the collected information, the goal was to transform the data in such a way that extreme data representing the darkest and brightest images would move to the center. The polynomial function we developed was

$$nL = L^3 \times (5.65e-06) - L^2 \times (1.53e-03) + L \times (7.98e-0.1) + 9.84\,, \qquad (5.2)$$

where nL is the new L^* value and L the original L^* value. The value results can be visualized in Fig 5.5, where the blue dots denote the transformed data values from the original image, which is represented by the red dots.

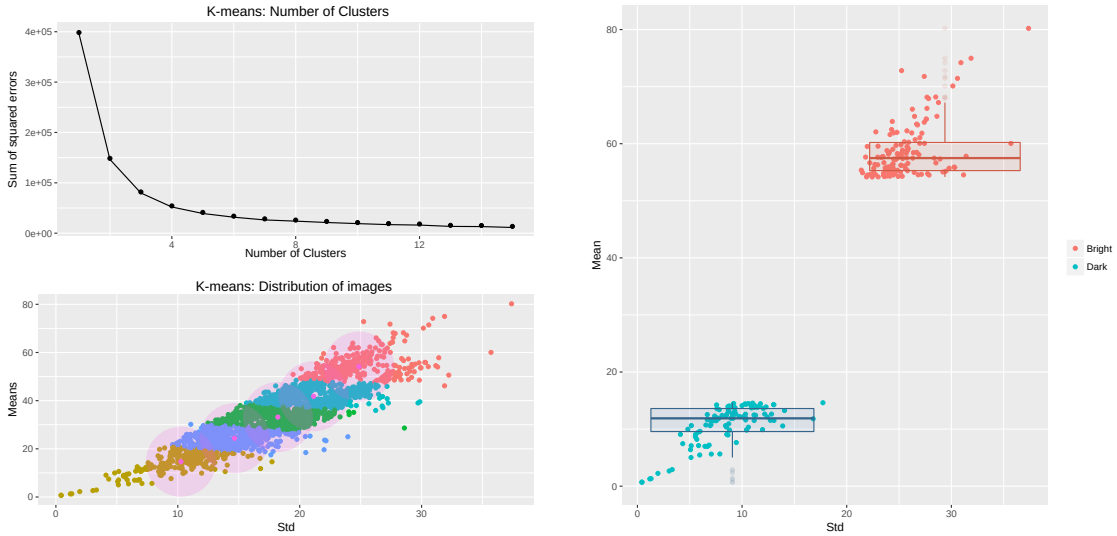

(a) K-means clustering Images

(b) Distribution L^* Channel on Clusters 1 & 5

Figure 5.4: L* Channel Distribution

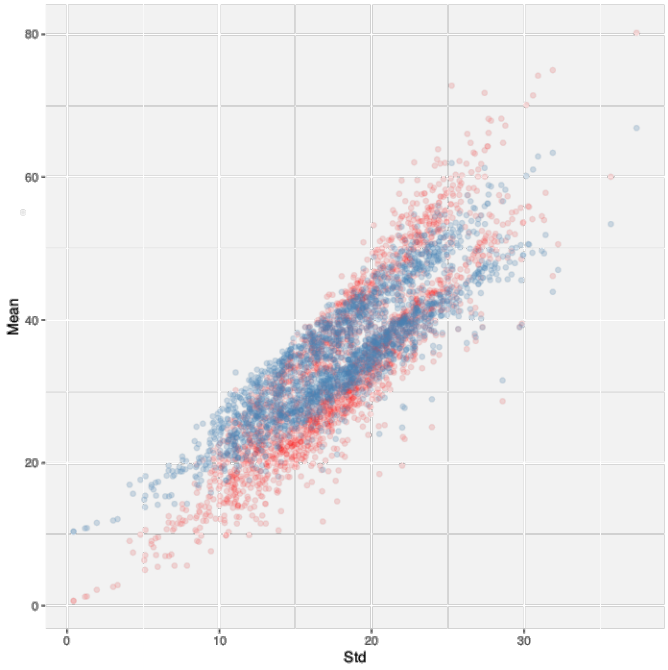

Figure 5.5: Distribution L* Channel on Clusters 1 & 5 Before and After Transformation

5.1.4

hspace1emReducing Color Variance

Just like any blood extravasation, the microaneurysm color goes through a sequence of changes, the most common sequence going from a bright red, to a brownish, to a yellowish color. Because our purpose was to enhance microaneurysms, we limited the scene in order to separate blood tissues from other structures using a novel approach.

After the normalization and the adjustment of the L^* values, we built a dataset with pixel values from vessels including microaneurysms and other structures like the optical disk, macula, exudates, and normal retina among others. Table 5.3 shows a wide range for a^* and b^* values and a difference in the vessels and background groups mean. In Fig. 5.6a each point represents the a* and b* pixels' values of the vessels and background pixels. In addition, there is a blue line separating the two groups that were obtained using the Linear Support Vector Machine, and two black points that are equidistant and orthogonal to the

svm plane. The new points are the centroids of the next transformation and represent a pixel value in the Lab color space. The euclidean distance of each pixel value over each centroid is calculated. Then, a division of these two values tells us which centroid is closest to this pixel value. Finally, the new pixel value was obtained after applying the following equation

$$npv = \begin{cases} ((pv - bed) \times rel) + bed, & \text{if rel} \quad <= 1 \\ ((pv - ved) \div rel) + ved, & \text{if rel} \quad > 1\,, \end{cases} \tag{5.3}$$

where pv is the pixel value of a^* and b^*, bed the Euclidean distance between the pixel value and the background centroid, ved the Euclidean distance between the pixel value and the vessel centroid, rel the division of $(\frac{bed}{ved})^4$, and npv the new pixel value. The new pixel values are displayed in Fig. 5.6b, and it is clear the centroids act as a magnet that attracts and brings the pixel values close to them. The results of the transformation can be corroborated visually, where the author can clearly distinguish between microaneurysms and the background. This was also proven in Fig. 5.6b where a better plane to separate these two groups can be visualized after the transformation.

Table 5.3: BACKGROUND & VESSELS PIXELS VALUES

	Vessels			Background		
	Mean	Std	Range	Mean	Std	Range
a*	10.90	5.71	35.30	16.59	4.25	38.55
b*	20.93	4.57	52.48	19.80	3.60	40.60

5.2 Slicing Images

Nowadays, it is difficult to process full size (2000 x 2000) images due to hardware limitations. Our approach is not to downsample the image size, but to crop the images with the lesions in it. If the average size of a micro-hemorrhage is 10x10 pixels and the size

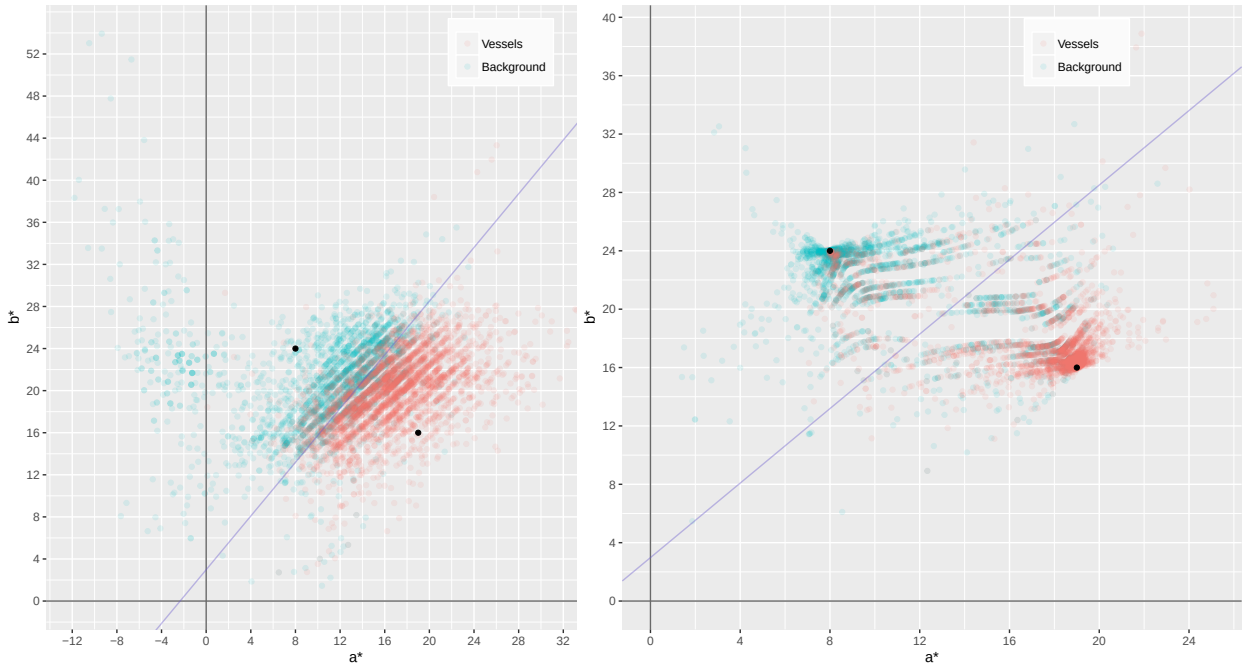

(a) Before Transformation (b) After Transformation

Figure 5.6: Distribution a^* & b^* Channels

of the images are 2000x2000 pixels, then downscaling the image to 500x500 pixels would decrease the lession to a size of 2x2 pixels, which would make it harder to detect any algorithm. After pre-processing the images, the approximate center of the lesion coordinates were located and we cropped the images into two different sizes: 60x60 pixels and 420x420 pixels. Each size represents a specific data set. In our initial part of the experiment, the images were obtained by cropping the images with and without the lesion in the center, once. We called this set *Dataset A* as shown in Table 5.4. Unbalanced data is shown with the majority of the cases in normal patients, which is an expected distribution due to the prevalence of DR. Training, tests, and validation cases for class zero consist of cropped images of normal images that include all the areas of the retina.

During the experiment, we increased the size of the training data as shown in Table 5.5 *Dataset B*. The purpose of this set was to evaluate how increasing the number of new pictures or increasing the number of cropped images that include lesions using augmenta-

Table 5.4: DATASET A

	60x60			420x420		
	Train	Validation	Testing	Train	Validation	Testing
Normal	10977063	453808	8240000	194276	8007	194260
Mild	4520	485	1881	4522	485	1887

tion [42] would impact the accuracy. Lately, for our final results we joined all the training cases, including annotated cases and augmented cases together, as shown in Table 5.6, and we labeled this set *Dataset C*. In Datasets B and C, the cases in the normal class were the same as in Dataset A.

Table 5.5: DATASET B

	Increasing Training Cases	
	With New Pictures	With Augmentation
60x60	7072	15798
420x420	6990	15765

Table 5.6: DATASET C

	Image Size	
	60x60	420x420
Total Images	41654	42259

5.3 CNN Architecture

Two independent types of architecture for the 60x60 sets in Table 5.7 and the 420x420 sets in Table 5.8 were created. The tables show the input size of each layer, the filter size, and the number of filters (Kernels). For all of the models, one stride for the filters

and padding was implemented. In our architecture, fractional max pooling [43] was implemented instead of classical maxpooling; the dropout rate was 0.1 instead of 0.5, the activation function was leakReLu [44, 45], the MSR approach was chosen [46] for the weight initialization, and batch normalization was performed after each convolution layer.

Table 5.7: MODELS 60X60

INPUT SIZE	MODEL A Filter w×h	MODEL A Num	MODEL B Filter w×h	MODEL B Num
60	3x3	64	3x3	64
			3x3	64
	FracMaxPool → *BatchNorm* → *LeReLU*			
45	3x3	128	3x3	128
			3x3	128
	FracMaxPool → *BatchNorm* → *LeReLU*			
30	3x3	256	3x3	256
			3x3	256
	FracMaxPool → *BatchNorm* → *LeReLU*			
23	3x3	512	3x3	512
			3x3	512
	FracMaxPool → *BatchNorm* → *LeReLU*			
15	3x3	1024	3x3	1024
			3x3	1204
	FracMaxPool → *BatchNorm* → *LeReLU*			
9	3x3	128	3x3	1536
			3x3	1536
	FracMaxPool → *BatchNorm* → *LeReLU*			
5	3x3	2048	3x3	2048
			3x3	2048
	FracMaxPool → *BatchNorm* → *LeReLU*			
	Dropout			
Full Conn		2048		
Full Conn		2048		
Full Conn		1024		
	LSF → NLL			

LSF LogSoftMax
NNL Negative Log Likelihood
LeReLu Leaked Rectified Linear Unit

Model **A** is a classic CNN model [4], while model **B** is a version of VGG [5]. Implementing classical VGG that includes more convolutions in each layer would dramatically reduce the size of the training batch in the 420x420 models, an unwanted side effect. In addition, our choice of fractional max pooling was due to the fact that the image sizes can be downsampled gradually, unlike maxpooling with 2x2 filters, where the next size is half

of the previous one.

For the classification phase, a variation of increasing the number of dropout layers and the rate of probability was implemented in model B as shown in Table 5.9. Furthermore, the performance of this model is compared with other models.

5.4 Feedback

The torch script applied to our experiments randomly chose between using a normal or mild DR class for the next input. After the group was selected, the script, once again, randomly chose a picture from the data pool of the class, making the processes completely stochastic. In addition, a feedback mechanism was created during training, in order to resend the images that were not classified correctly.

The difference of the values between the current loss function and that of the prior batch greater than zero indicates that the current batch did not classify as well as the previous batch. This is the basis of our feedback function. The function created for the feedback detects the batch in which the current difference of the values of the cost function surpass the moving average of the mean of the differences of the previous batches. The polynomial function used in our feedback is as follows:

$$\begin{aligned} cve = bn^4 \times (-1.41e-20) + bn^3 \times (2.08e-15) + bn^2 \\ \times -(9.84e-11) + bn \times 6.27e-07 + (1.50e-01)\,, \end{aligned} \tag{5.4}$$

where bn is the batch number and cve the cost value expected. If the cost value of the batch during the training was greater than we expected it to be after applying the equation 5.4, we resent the same batch for re-training as shown in Fig. 5.7.

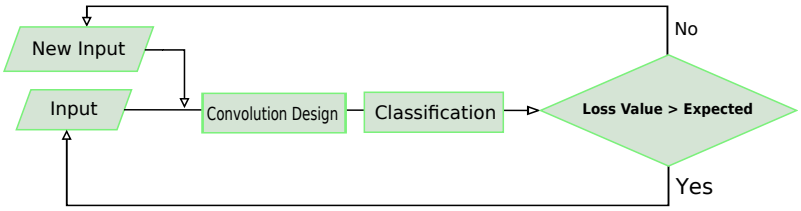

Figure 5.7: Feedback

5.5 Monitoring

The original torch script provided the values of the loss function accuracy and the confusion table for each epoch, where those values were the result of averaging all of the batches' values. Also, the script processed the loss and accuracy values for each epoch in the validation set. Then, we ran the final updated weights of the trained CNN in the validation, training, and testing sets to obtain the probability of all the images. Once we had the probability and the labels of the images, we could construct all confusion tables.

For the initial part of the experiment, the loss and accuracy of the training, the validation, and the testing sets were used to choose the most efficient model. For our final experiment, after training the more accurate CNN model, the weights of the trained CNN at regular intervals were kept. Using those weights, the probability of each image in the testing sets was obtained. Then, ROC analysis was used to get the cut-off of the probability values used to recieve the maximum specificity or sensitivity of the 420x420 or 60x60 sets, respectively. Finally, the most accurate weights of the CNNs given by the ROC analysis were used to obtain the probabilities of the Diabetic Retinopathy Database and Evaluation Protocol, which were used to compare the overall probabilities to the ground truth.

The identification of the images sent to the training was recorded in a log file for further analysis. As expected, the monitoring process showed that the ratio of normal and mild pictures used during the training process was $\approx 1.02 - 1.04$. It is also evident that that

the number of repeated images of the mild class was bigger than the number of repeated images of the normal class due to their pool-size.

5.5.1

hspace1emROC

ROC [38] is a graphical representation of discriminatory tests over two populations where the *x-axis* represents the sensitivity, the *y-axis* represents $1 - specificity$, and the curve shows all threshold values. Several indexes were developed to summarize ROC in one value such as the area under ROC. Also, a method to find the optimal cut point, where sensitivity and specificity are maximized, such as the Younden Index was used in this study. Youndex Index is the minimimun Euclidean distance of the top left corner, where sensitivity and specificity are equal to one, and the ROC curve. The package OptimalCutpoints [1], from Rcran was used to obtain the optimal points of the max sensitivity and specificity.

[1] https://cran.r-project.org/web/packages/OptimalCutpoints/index.html

Table 5.8: MODELS 420X420

INPUT SIZE	MODEL A Filter w×h	Num	MODEL B Filter w×h	Num
420	3x3	32	3x3	32
			3x3	32
FracMaxPool → BatchNorm → LeReLU				
360	3x3	48	3x3	48
			3x3	48
FracMaxPool → BatchNorm → LeReLU				
300	3x3	46	3x3	64
			3x3	64
FracMaxPool → BatchNorm→ LeReLU				
240	3x3	72	3x3	72
			3x3	72
FracMaxPool → BatchNorm→ LeReLU				
180	3x3	96	3x3	96
			3x3	96
FracMaxPool → BatchNorm→ LeReLU				
120	3x3	128	3x3	128
			3x3	128
FracMaxPool → BatchNorm→ LeReLU				
60	3x3	48	3x3	190
			3x3	190
FracMaxPool → BatchNorm→ LeReLU				
45	3x3	256	3x3	256
			3x3	256
FracMaxPool → BatchNorm→ LeReLU				
30	3x3	348	3x3	348
			3x3	348
FracMaxPool → BatchNorm→ LeReLU				
23	3x3	512	3x3	512
			3x3	512
FracMaxPool → BatchNorm→ LeReLU				
15	3x3	1024	3x3	1024
			3x3	1024
FracMaxPool → BatchNorm→ LeReLU				
9	3x3	1536	3x3	1536
			3x3	1536
FracMaxPool → BatchNorm→ LeReLU				
5	3x3	2048	3x3	2048
			3x3	2048
Dropout				
Full Conn		2048		
Full Conn		2048		
Full Conn		1024		
LSF→ NLL				

LSF	LogSoftMax
NNL	Negative Log Likelihood
LeReLu	Leaked Rectified Linear Unit

Table 5.9: DROPOUT SETTING

Dropout	0.5
Full Conn	2048
Dropout	0.5
Full Conn	2048
Dropout	0.5
Full Conn	1024
LSF $\rightarrow$ NNL	

CHAPTER 6

EXPERIMENTAL DESIGN AND RESULTS

For this study, we divided the CNN in 4 phases. The first phase is the input-phase, where input processing used to enhance features and augmentation of the dataset is performed. The second phase is the Convolution Design-phase, where modifications to the number of convolutions and filters can be completed. Variation of the type of pooling, normalization,and neural activation function is also possible in this stage. The classification-phase or the third phase, includes full-connected layers with the neural activation function and loss function. The dropout of nodes in a full-connected layer in this phase has been a common modification, in recent studies. The fourth phase is the training-phase, where we can alter the hyper-parameters, learning algorithms, and perform feedback. Following pedantic rules, each phase should be evaluated separately, in order to measure the impact of changing a parameter on that phase, though changing only a parameter at any point is often unpractical.

Our plan for the study was to select the modifications in the input, convolution design, classification, and training phase that would improve our sensitivity and specificity in the training, validation, and testing sets. Dataset C was trained with all the previous modifications, in order to get the weights that performed best in the testing sets and the cutoff point values provided by ROC analysis to achieve the optimal sensitivity and specificity. Finally, the Diabetic Retinopathy Database and Evaluation Protocol dataset was tested and the results were compared to their own groundtruth.

6.1 Modifying Input Quality & Architecture

6.1.1

hspace1emDesign

Initially, we evaluated how CNN performed in Models A and B using both raw data and pre-processed images from Dataset A (Table 5.4) as displayed in Fig. 6.1. Here, we evaluated the accuracy of the confusion table in the training and validation sets, by changing the quality in the input-phase and the model in the architecture-phase. The more accurate model and image set are used for the next stage.

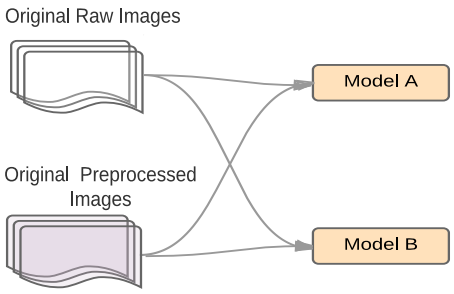

Figure 6.1: Raw vs Pre-processed Images for Model A & B

6.1.2

hspace1emResults

Table 6.1 displays the contingency table and the accuracy plot of the images with a size of 420x420 in the training set. Pre-processed images trained with Model B reached a better accuracy with less epochs than the other models as shown in Table 6.1. It is also illustrated processed images perform better than raw images, and that all images and models could reach a similar accuracy if the number of epochs increases. When using raw images for Model A, the training was suspended, due to of the slow increase in the slope. It is notable that processed images reached a 90 in accuracy in the first 100 epochs and the slope was

steeper in the first 50 epochs. However, during the last 150 epochs in the processed images, the increase in the accuracy was a minimum.

Table 6.1: RAW VS PRE-PROCESSED IMAGES FOR MODEL A & B ON 420 × 420 SET

		PREDICTIONS: PERCENTAGE BY ROW							
		STANDARD CNN				VGG CNN			
		Raw Image 250 Epochs		*Processed Image 300 Epochs*		*Raw Image 365 Epochs*		*Processed Image 250 Epochs*	
		Mild	**Normal**	**Mild**	**Normal**	**Mild**	**Normal**	**Mild**	**Normal**
TRUE	**Mild**	84.431	15.569	98.6831	1.369	97.851	2.149	98.722	1.278
	Normal	21.092	78.908	2.244	97.756	3.254	96.746	1.77	98.230

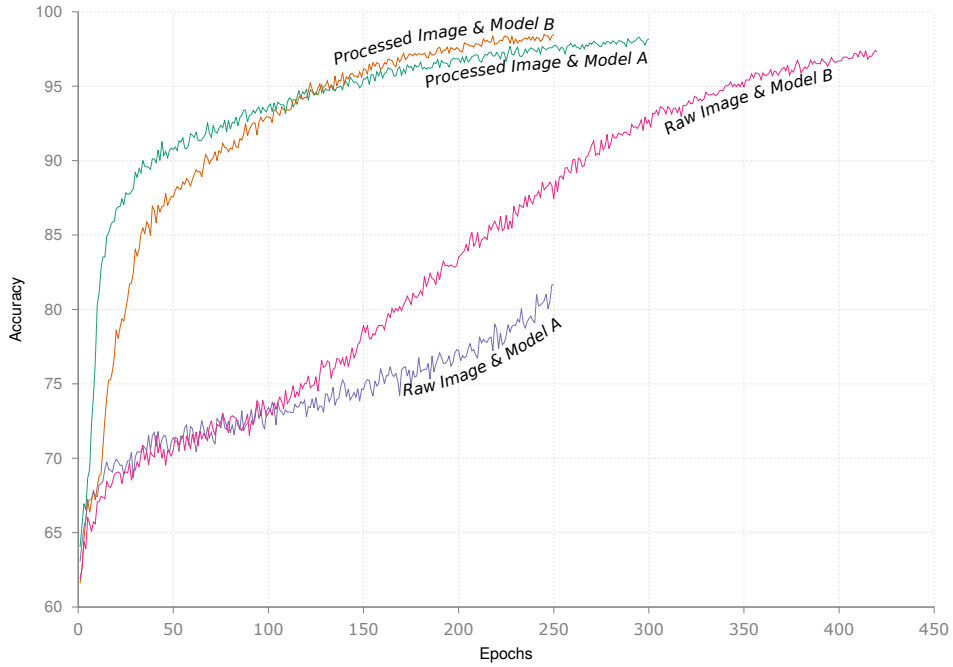

Table 6.2 shows the contingency table and the accuracy plot of the 60x60 image sets in the training set. It is evident that Model B performed better than Model A, and that Model A reaches a similar accuracy with raw pictures than the other models, but only after a long training (300 epochs). It is also noticeable that most of the accuracy was achieved in the first 50 epochs using processed images, with a steeper slope in the first twenty epochs.

Comparing the 60x60 image set to the 420x420 image set, the first reaches a higher accuracy in all the models with less training. In addition, it is visible that Model B outperforms Model A. For the next step, Model B and pre-processed images were chosen.

Table 6.2: RAW VS PRE-PROCESSED IMAGES FOR MODEL A & B ON 60 × 60 SET

		PREDICTIONS: PERCENTAGE BY ROW							
		STANDARD CNN				VGG CNN			
		Raw Image 300 Epochs		*Processed Image 180 Epochs*		*Raw Image 180 Epochs*		*Processed Image 180 Epochs*	
		Mild	**Normal**	**Mild**	**Normal**	**Mild**	**Normal**	**Mild**	**Normal**
TRUE	**Mild**	98.581	1.419	98.576	1.424	99.234	0.766	99.343	0.657
	Normal	2.08	97.920	1.841	98.159	1.714	98.286	1.269	98.731

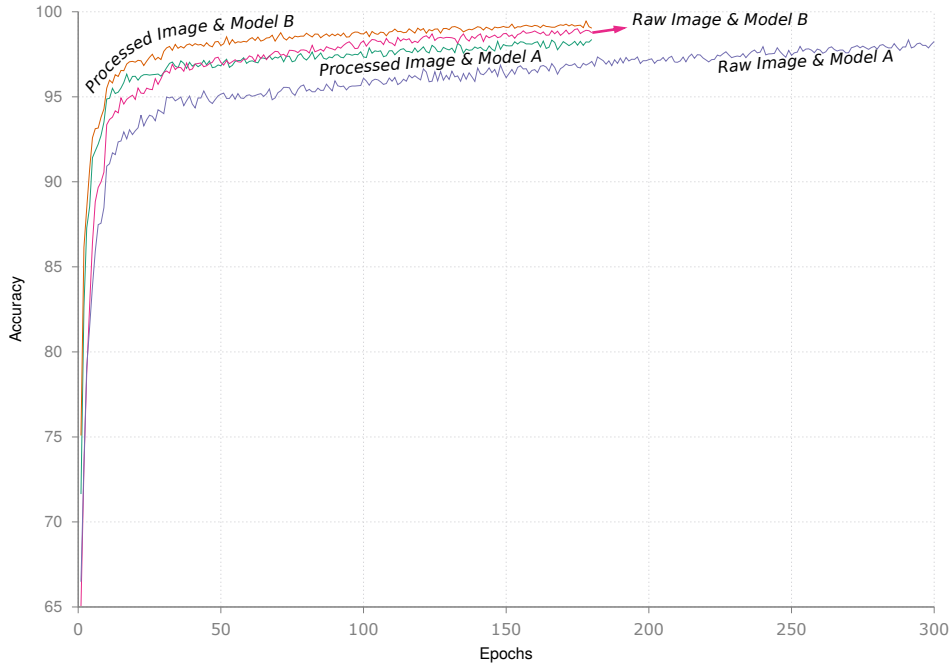

6.2 Modifying Classification & Training

6.2.1

hspace1emDesign

Fig. 6.2 depicts an stage that compares the effects of feedback in pre-processed images using Model B against an increase in the dropout layers and dropout probability to 0.5 in the pre-processed images. Here, we looked for the effects of making changes in the classification-phase versus training-phase in sensitivity and specificity, using training and testing sets from Dataset A.

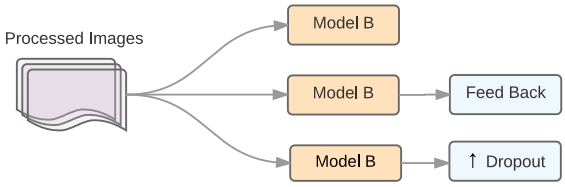

Figure 6.2: Feedback vs Dropout

6.2.2

hspace1emResults

Fig. 6.3 shows the absence of significant differences in accuracy between the training using model B with a dropout probability of 0.1 (vanilla), the training increasing the dropout probability to 0.5 and dropout layers, and the training increasing the feedback in both the 60x60 and 420x420 sets. The accuracy is over 95 for all of the sets, and over-fitting is presented in the validation sets. For a 60x60 set, the crossing point between the training and testing lines using validation set is reached when the accuracy is 90 for the 60x60 set and 82 for the 420x420 set.

Table 6.3 and Table 6.4 show the values of the sensitivity and specificity of the train-

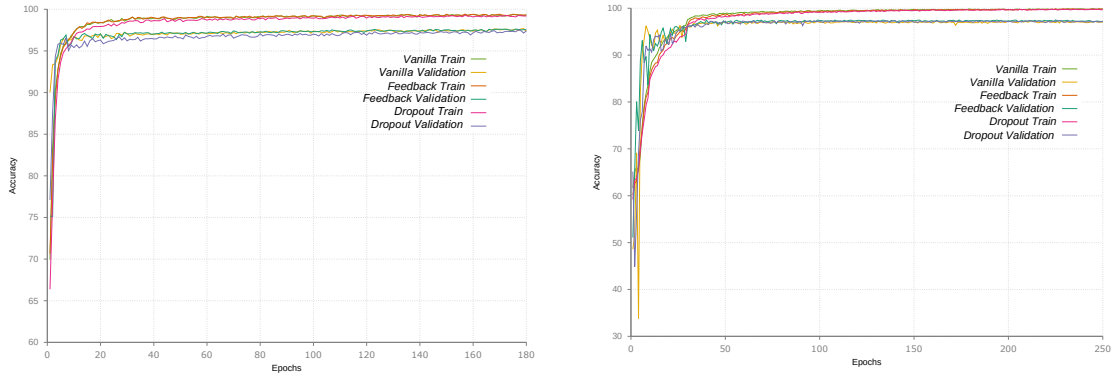

(a) Image Size 60x60

(b) Image Size 420x420

Figure 6.3: Feedback Vs Dropout Accuracy

ing and test sets in Dataset A. The sensitivity and specificity of the 60x60 images were satisfactory for both sets with a small decrease in the values compared to the training set. Also, a higher sensitivity is visible in test sets when increasing the dropout. However, for the 420x420 sets, the sensitivity decreased significantly, becoming more prominent when increasing the dropout layers and probability.

Notice that the training was not stopped as soon as over-fitting was detected and that the weights used to get those values belonged to the last epoch in training.

Table 6.3: FEEDBACK VS INCREASING DROPOUT TRAINING SET

	60X60 180 EPOCHS			420X420 250 EPOCHS		
	Vanilla	*Feedback*	*Dropout*	*Vanilla*	*Feedback*	*Dropout*
Sensitivity	99	99	99	99	99	98
Specificity	99	99	98	97	97	99

For the next phase of the experiment our goal was to increase the sensitivity in the 420x420 set. We used the pre-processed images, Model B, and Feedback mechanism.

Table 6.4: FEEBACK VS INVREASING DROPOUT TESTING SET

	60X60 180 EPOCHS			420X420 250 EPOCHS		
	Vanilla	*Feedback*	*Dropout*	*Vanilla*	*Feedback*	*Dropout*
Sensitivity	92	92	96	62	67	61
Specificity	99	99	98	97	97	99

6.3 Modifying Input Quantity

6.3.1

hspace1emDesign

Fig 6.4 illustrates the design comparing the changes corresponding to increases in size of input by using augmentation against increases in size of input by adding new images to the dataset (Dataset B), where the previous stage performed better in the 420x420 set. The performance is evaluated by measuring the sensitivity and specificity of the testing set using different epochs.

Of the new cases provided by the Messidor dataset, 1276 were added to the 60x60 set and 1199 were added to the 420x420 set. Dataset B consists of the new cases and cropped images with the lesion not centered. The augmentation set consists of images from Dataset A and six cropped images with the lesion not centered assuring that the images are completely different.

6.3.2

hspace1emResults

The accuracy plot of the training set in Fig. 6.5 shows that the input augmentation reached a higher accuracy than the new input at the beginning of the training, but at the

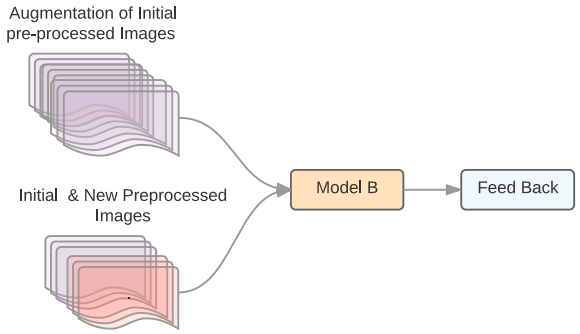

Figure 6.4: Augmentation vs New Images

end of the process both achieved a similar accuracy. The plot also displays over-fitting on validation sets for both the input augmentation and the new input sets. In addition, Fig. 6.5 shows a difference in the crossing point between the training and the validation sets, by taking more epochs, when using the new input.

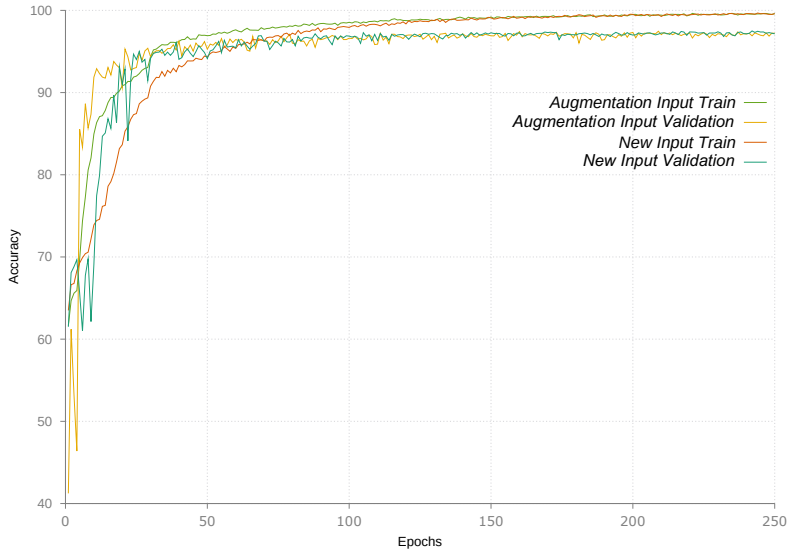

Figure 6.5: Augmentation vs New Input Accuracy

The sensitivity increases dramatically in both sets by adding either new data or using input augmentation in the testing sets as shown in Table 6.5. This increase is larger in input augmentation compared to the new input. In early epochs, before over-fitting is present, the sensitivity is also better. One aspect that should be considered, is that for Dataset B the input augmentation set is twice as large as the new input set.

Table 6.5: INPUT AUGMENTATION VS NEW INPUT SENSITIVITY & SPECIFICITY

		Augmentation		New Input	
		Sensitivity	Specificity	Sensitivity	Specificity
Epochs	50	82	94	79	94
	100	79	96	76	97
	150	73	98	71	98
	200	68	99	72	99
	250	74	99	72	99

Although the sensitivity has improved, it can be further improved by either modifying the input or modifying the architecture. With the original and new inputs, we created a new dataset, Dataset C, which contains the original images and the same images cropped by factor of 10 with the lesion dispersed in different regions of the image as shown in Fig. 6.6. We trained Dataset C with model B and Feedback. We also kept the weights for every 50 epochs in images that have a size of 420x420 and the weights for every 20 epochs in images that have a size of 60x60.

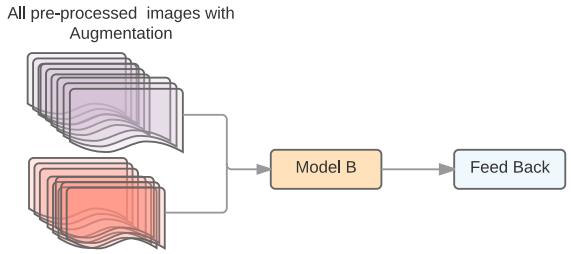

Figure 6.6: Final Input

The accuracy of training Dataset C with model B and feedback is shown in Fig 6.7. Images that have a size of 60x60 will reach a higher accuracy than images with a size of 420x420. In addition, over-fitting is more prominent in the 420x420 image sets.

Table 6.7 shows the sensitivity and specificity acquired with having the weights at different epochs in the test dataset. The highest sensitivity and specificity are reached with weights of epochs 40 and 50 in the 60x60 sets and 420x420 sets and are more accurate than

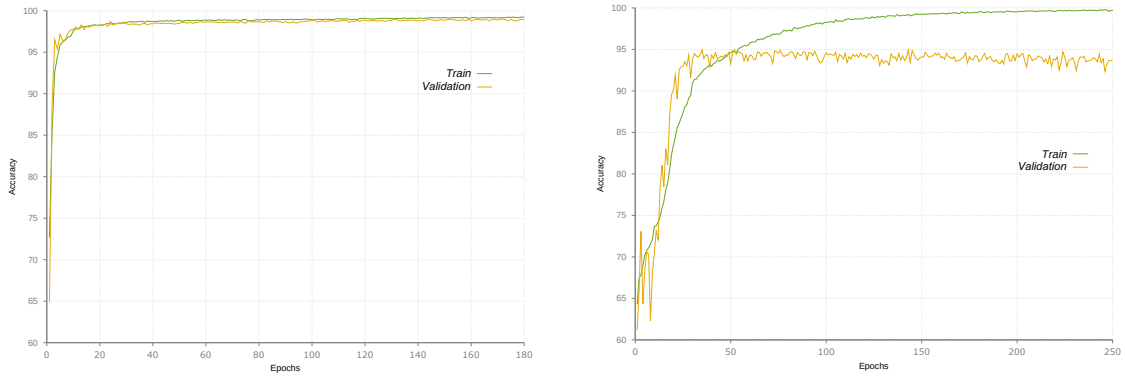

(a) Image Size 60x60 (b) Image Size 420x420

Figure 6.7: Final Input Accuracy

those shown in Table 6.5. A decrease in the sensitivity of both sets occurs with a higher number of epochs as presented in Table 6.7. This supports the over-fitting findings in the validation set depicted in Fig. 6.7. The weights that produce the best sensitivity for the 420x420 set and the best specificity for the 60x60 set are chosen in the next phase of the study.

Table 6.6: FINAL INPUT SENSITIVITY & SPECIFICITY

	60x60			420x420	
	Sensitivity	Specificity		Sensitivity	Specificity
Epochs 20	93	97	Epochs 50	88	95
40	93	98	100	79	98
60	91	98	150	75	99
80	92	98	200	76	99
100	91	98	150	71	99
120	90	98			
140	92	99			
160	91	98			
180	91	98			

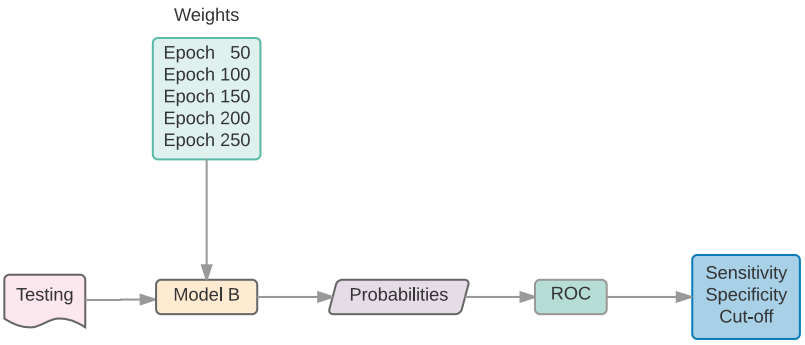

Figure 6.8: Cutoff

6.4 ROC Analysis

6.4.1

hspace1emDesign

After having run the CNN in the testing set and finding the probability of each image in each category (normal & microaneurysms), the sensitivity, specificity, and optimal cut-point values were obtained by applying ROC to the testing set as shown in Fig. 6.8. Later, we ran our CNN model with the weights that provided the best accuracy and sensitivity in the Diabetic Retinopathy Database and Evaluation dataset to determine how the model performed overall

6.4.2

hspace1emResults

Table 6.7 shows that for the 60x60 set, the values of the sensitivity and specificity are similar at different cut-off points, with epoch **80** providing a slightly higher specificity. For the 420x420 dataset, epoch **50** displays the best accuracy and sensitivity. Those epochs were used for further analysis.

Table 6.7: ROC CUTOFF

	60x60					420x420				
	Epochs	Cutoff	Sensitivity	Specificity	Accuracy	Epochs	Cutoff	Sensitivity	Specificity	Acuracy
	20	.27	95	97	96	50	.32	91	93	91
	40	.18	95	97	96	100	.02	90	93	91
	60	.09	95	97	96	150	.01	89	93	90
	80	.13	95	98	96	200	.01	89	94	90
	100	.06	95	97	96	1250	.01	88	93	90
	120	.06	95	97	95					
	140	.11	95	97	95					
	160	.05	95	97	95					
	180	.04	95	97	95					

Fig. 6.9 shows a ROC analysis, with an area under the curve of 0.9828, 0.9621 for the 60x60 and 420x420 datasets. Fig. 6.9 also displays a variation in the accuracy, by having different cutoff points. For the 60x60 set, a acceptable specificity was reached with a cutoff at 0.9, without sacrificing the accuracy greatly. For the 420x420 set, we set the cutoff point to be at 0.10 and achieved a high sensitivity without sacrificing the accuracy.

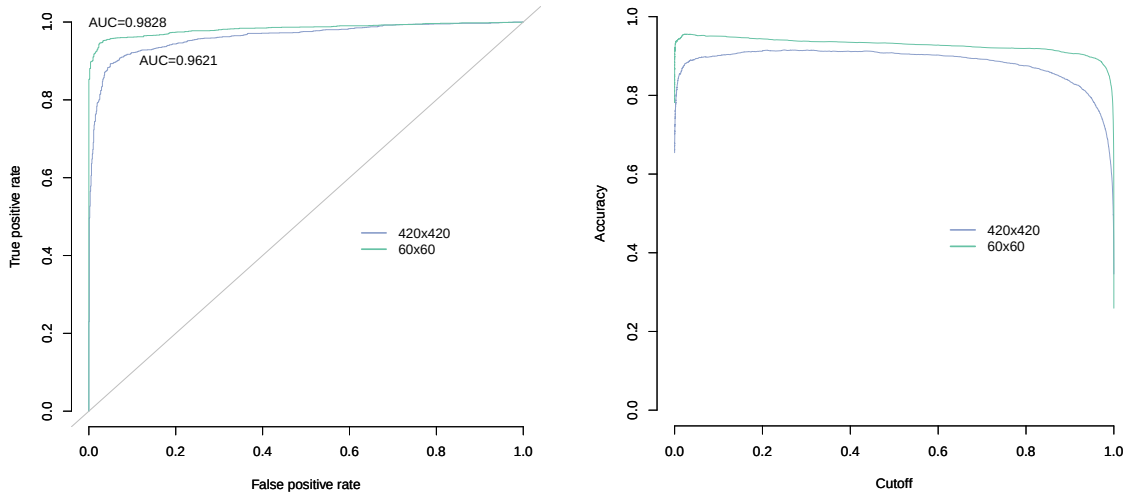

(a) ROC

(b) Accuracy Vs Cutoff

Figure 6.9: ROC & Accuracy Vs Cutoff Point

The pictures from the DiaRetDB1 were sliced into sizes of 60x60 and 420x420. After getting the probabilities for each slice, we visually evaluated the lesions found by the CNN

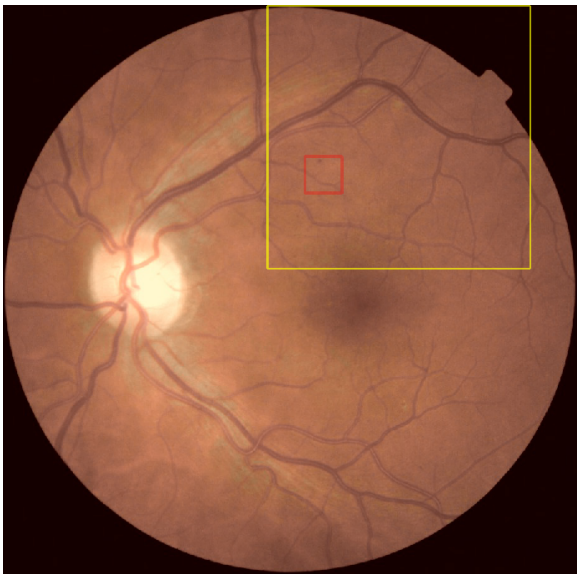

Figure 6.10: Final Image Result

and compared them to the groundtruth lesions provided by the database. The results of the twenty pictures with 51 lesions are shown in Table 6.8, which states that model B of the CNN in 60x60 and 420x420 sets detects most of the lesions but there are still a number of false positives in the 60x60 set. If the 420x420 CNN model is running to detect the lesions first and the the 60x60 model is running over those positives, the number of false positives decreases, holding the true positive cases.

Table 6.8: DIARETDB1 INPUT

51 Lesions From Dataset C

	Cut off	TP	FP	FN
60x60	.90	49	385	2
420x420	.10	49	6	2
First: 420x420 Next:60x60	.10 .90	49	129	2

In Fig. 6.10 the yellow square represents the true positive 420x420 image, and the small red square represents the true positive 60x60 image. The lesion is shown close to the top border.

CHAPTER 7

DISCUSSION

Qualitative improvement of the image not only facilitates the detection of the lesions for annotations, but also decreases the number of epochs needed to reach a high accuracy for training and validation sets. The benefits of shortening the training time are economic, environmental, and human and can be reflected in the cost reduction. Because the color of microaneurysms are located between 650-570 nm in the light spectrum and it is not possible to find cyan colored microaneurysms, color reduction plays a significant role in medical images where its variance is limited. As an illustration, the function in equation 5.3 was successfully applied to enhance the lesions and provide contrast against their surroundings.

Quantitative gain either by augmentation or with new images makes the process more accurate. Deep learning is very dependent of the size of the data. However, sometimes the data-sets are limited, so augmentation was introduced to overcome this difficulty. Although augmentation increased the accuracy of the study, adding new images had the same effect, but with a lower number of images. Using Dataset C, we achieved a better accuracy compared to Dataset B, but the increase in the accuracy was not as high as the one between Dataset A and B. This provides evidence that augmentation has a limit in improving accuracy, but more studies are still needed.

The idea of having two different sized datasets (420x420 and 60x60) came from an old medical tradition, which is explained as follows. Syphilis was a very dangerous disease in the early 19th century, that later on had unpleasant complications. Epidemiologists came up with the idea of a test (VDRL) that would detect all the cases of the disease. However,

it would produce a lot of false positives. The patient, whose VDRL test was positive, required a second test named (FTA-ABS), which had a specificity that was almost perfect, but without a high sensitivity. Economic, logistic, and epidemiological reasons support this approach. Although we used the same methodology, CNN, for both sets (60x60 and 420x420) they differ in the model and input size. As a result, these models could be considered different types of tests. The efforts in the study to increase the sensitivity in the 420x420 set by increasing the input size and implementing feedback were well paid off by diminishing the false positives generated, when CNNs were applied to cropped images with a size of 60x60 pixels as a unique test.

Most of the DR studies have been focused on classifying its stages, rather than identifying the specific lesion. R-CNN, Fast R-CNN,and Faster R-CNN have been used for object localization with excellent results, but this still has not solved the problem for small objects. Karphaty [47], introduced the idea of foveal stream for video classification by cropping the image stream into its center. Grinsven's work [20] developed a selective data sampling for the detection of hemorrhages, where the lesions were placed in the center of a cropped image of 41x41 pixels. Although the fovea in the retina has a more concentrated area with photo-receptors, it is the attention that defines the discrimination of the objects. In a similar way, we proposed that keeping the same resolution of the image, but cropping the image to the object of interest would simulate the attention. Cropping the image with the lesion in different positions of the image gives the input data a higher variance. We also made sure to avoid that the CNN would learn the center position instead of the features of the lesion itself.

In the 420x420 set, applying feedback to the CNN performed better than vanilla and dropout increasing. Most of the chemical or physiological pathways have a feedback mechanism to regulate its response to a specific stimulus. Our approach tried to find the batch with mild and normal classes that perform poorly after back-propagation to retrain them

again. One of the limitations of this approach was that we needed to know the values of the loss function per batch during all of the training in order to calculate the function. However, it is possible that a dynamic process can be created using a number of previous batches to get the threshold and update it after a certain number of batches. Grinsven's work [20] proposed a feedback method that assigns a probability score to each pixel and is modified when "the probability scores differs the most from the initial reference level",so the higher the weight probability the higher the chance of it being selected. One drawback of this methodology is that it is only applied to the negative sample.

Some observations that called the our group's attention was that the CNN selected some small artifacts as lesions. Also, the algorithms selected small groups of lesions, but when a bigger number of lesions were grouped in such a way that they mimic hemorrhages, they were not detected. Although we gained some progress in the detection and selection of microaneurysms and our technique's performance surpassed all of the methods in the literature at this time, there are still a number of false positives.

CHAPTER 8

CONCLUSIONS

This study proposed a novel methodology for pre-processing images that would decrease the training time and improve the quality of the images for annotations. Normalization is the first step in image pre-processing that generates an image with a mean value closer to the mean value of all of the images, and with a standard deviation value bigger than its original value. The second step adjusts the luminescence of the images, so that the dark and white regions would be more visually appealing. The final step is color reduction,where the intensity of the pixels of the colors is moved within the spectrum between the yellow and orange intensity. The new intensity of the pixels' image is similar to either the vessel color or to the background color.

Also, the study reaffirms that deep learning is data dependent and obtain new data is as important as augmentation. Some datasets have a limited number of cases that need to be trained by a Deep Learining algorithm. Augmentation is a methodology that overcomes this limitation, and has been used successfully in several studies. The study showed that augmentation has a limitation when improving accuracy and adding new cases to the data set and performs better than using augmentation. Therefore, in future studies augmentation should be used in a cautionary manner.

The study offered new feedback methodology for training that improves accuracy in the 420x420 testing set. Finally, the study proposed a novel methodology by using a multiscale CNN model that increases the performance for identification and classification of microanuerysms, which represent small sections of of the scene. Thus, this study combined

a CNN with a high sensitivity and a CNN with a high specificity to detect microaneurysms with a few false positives. CNN trained with images that have a size of 60 $\times$ 60 pixels to detect mycroaneurysms, artifacts, and hemorrhages. In addition, a CNN trained with images that have a size of 60 $\times$ 60 pixels detected normal areas in our eyes, but they had some features that triggered the CNN. On the other hand, a CNN trained with images having a size of 420 $\times$ 420 pixels possessed a bigger area that makes it difficult to distinguish small lesions from normal lesions. However, the study reached a sensitivity of 91% and specificity of 93% for this CNN. This study used both CNNs sequentially to obtain our more accurate results.

APPENDIX A

SOFTWARE IMPLEMENTATION

Image preprocessing helped to reduce the training time measured by the number of epochs need to have the highest accuracy during training. Also, preprocessing helps the author to make annotations in the images. The next section describes the manner our research group implemented the algorithms explain in the methods chapter.

A.1 Preprocessing

For the study a well known, popular, good quality, and open source framework was chosen,OpenCV. API's framework provides several classes for loading, transform, conversion, and drawing images, and we took advance of them. Also a simple GUI to display the results of the operation and trackbars to make dynamic changes are available in this frame work. Initially the image is loaded from a file; OpenCV provides MAT class to storage the image as shown in the line 3.

```
1  string im= "image name";
2  Mat image;
3  image = imread(im);
```

After loading the image, conversion to float values is performed in the line 5. Then, color space transformation from RGB to L^*, a^*, b^* is showed in the line 6. The values of the means and standard deviation of all pictures, and for each channel are assigned to variables as depicted in the lines 7 to 12. In the lines 14 to 19 variables holding the mean

and standard deviation for each channel and for one image are assigned. The variable for the coordinates of the background centroid and vessel centroid are defined and assigned in the lines 20 and 21 respectively.

```
4  image.convertTo(fimage, CV_32F, 1.0/255.0,0);
5  cvtColor(fimage,labimage,CV_BGR2Lab);
6  Scalar mean(0.0,0.0,0.0,0.0),stddev(0.0,0.0,0.0,0.0);
7  meanStdDev(image,mean,stddev)
8  float meanAllImL= 37.62;
9  float meanAllIma= 11.75;
10 float meanAllImb= 19.26;
11 float stdAllImL=  19.54;
12 float stdAllIma=  8.70;
13 float stdAllImb=  11.40;
14 float meanImL= mean[0];
15 float maanIma= mean[1];
16 float meanImb= mean[2];
17 float stdImL= std[0];
18 float stdIma= std[1];
19 float stdImb= std[2];
20 float xc1=8.0961, yc1=24.542;
21 float xc2=19,yc2=16;
```

A loop for each row and column to get the value of each pixel and channel is performed as shown from lines 22-24; the intensity values for each pixels are assigned to a variable in lines 24-27. Normalization of the channel L is executed in line 28, followed by lightness adjustment in the line 29. Normalization for channel a^* and b^* is performed in the lines 33 to 36. The euclidean distance is calculate for the pixel value to each centroid. Lines 43 t0 48 describe the function to transform the pixel value based on the proximate to the background or vessel.

```
22      for (int i = 0; i < labimage.rows; i++){
23      float* data=labimage.ptr<float>(i);
24      for (int j = 0; j < labimage.cols ; j++){
25      float d0=(data[(3*j)+0]);
26      float d1=(data[(3*j)+1]);
27      float d2=(data[(3*j)+2]);
28      float tmpl = (((d0-m0)*((sumstddev[0]/s[0])*2))+m0)+(summean[0]-m0);
29      float tmp2 = (pow(tmpl,3) * 0.0000056656) -(pow(tmpl,2) *
30      0.0015297)+ (tmpl*0.7973646)+ 9.83683 ;
31      float tmpa = (((d1-m1)*(sumstddev[1]/s[1]))+m1)+ (summean[1]-m1);
32      float tmpb = (((d2-m2)*(sumstddev[2]/s[2]))+m2)+(summean[2]-m2);
33      float r1= pow((pow((tmpa-xc1),2)) + (pow((tmpb-yc1),2)),0.5);
34      float r2= pow((pow((tmpa-xc2),2)) + (pow((tmpb-yc2),2)),0.5);
35      float rel=pow((r1/r2),4);
36      data[(3*j)+0]=tmp2;
37      if (rel <= 1){
38      data[(3*j)+1]= ((tmpa-xc1)*rel)+xc1;
39      data[(3*j)+2]= ((tmpb-yc1)*rel)+yc1;
40      }else{
41      data[(3*j)+1]= ((tmpa-xc2)/rel)+xc2;
42      data[(3*j)+2]= ((tmpb-yc2)/rel)+yc2;
43      }
44      }
45     }
```

REFERENCES

[1] M. Yanoff and J. S. Duker, *Ophthalmology*. Edinburgh: Mosby, 2008.

[2] C. P. Wilkinson, F. L. I. Ferris, R. E. Klein, P. P. Lee, C. D. Agardh, M. Davis, D. Dills, A. Kampik, R. Pararajasegaram, and J. T. Verdaguer, "Proposed international clinical diabetic retinopathy and diabetic macular edema disease severity scales," *Ophthalmology*, vol. 110, no. 9, pp. 1677–1682, 2003.

[3] Y. LeCun, O. Matan, B. Boser, J. S. Denker, D. Henderson, R. E. Howard, W. Hubbard, L. D. Jackel, and H. S. Baird, "Handwritten zip code recognition with multilayer networks," in *Proc. of the International Conference on Pattern Recognition*, IAPR, Ed., invited paper, vol. II, Atlantic City: IEEE, 1990, pp. 35–40.

[4] A. Krizhevsky, I. Sutskever, and G. E. Hinton, "Imagenet classification with deep convolutional neural networks," in *Advances in Neural Information Processing Systems 25*, F. Pereira, C. Burges, L. Bottou, and K. Weinberger, Eds., Curran Associates, Inc., 2012, pp. 1097–1105.

[5] K. Simonyan and A. Zisserman, "Very deep convolutional networks for large-scale image recognition," *CoRR*, vol. abs/1409.1556, 2014.

[6] S. Zagoruyko and N. Komodakis, "Wide residual networks," *CoRR*, 1999. arXiv: 1605.07146 [cs.CV].

[7] C. Szegedy, W. Liu, Y. Jia, P. Sermanet, S. Reed, D. Anguelov, D. Erhan, V. Vanhoucke, and A. Rabinovich, "Going deeper with convolutions," *CoRR*, 1999. arXiv: 1409.4842 [cs.CV].

[8] X. Glorot and Y. Bengio, "Understanding the difficulty of training deep feedforward neural networks," *JMLR*, 2010.

[9] S. Ioffe and C. Szegedy, "Batch normalization: Accelerating deep network training by reducing internal covariate shift," *CoRR*, 1999. arXiv: 1502.03167 [cs.LG].

[10] I. J. Goodfellow, D. Warde-Farley, M. Mirza, A. C. Courville, and Y. Bengio, "Maxout networks," *CoRR*, vol. abs/1302.4389, 2013.

[11] H. Su, F. Liu, Y. Xie, F. Xing, S. Meyyappan, and L. Yang, "Region segmentation in histopathological breast cancer images using deep convolutional neural network,"

in *2015 IEEE 12th International Symposium on Biomedical Imaging (ISBI)*, 2015, pp. 55–58.

[12] E. E. Nithila and S. Kumar, "Automatic detection of solitary pulmonary nodules using swarm intelligence optimized neural networks on {ct} images," *Engineering Science and Technology, an International Journal*, pp. –, 2016.

[13] V. Gulshan, L. Peng, M. Coram, M. C. Stumpe, D. Wu, A. Narayanaswamy, S. Venugopalan, K. Widner, T. Madams, J. Cuadros, R. Kim, R. Raman, P. C. Nelson, J. L. Mega, and D. R. Webster, "Development and validation of a deep learning algorithm for detection of diabetic retinopathy in retinal fundus photographs," *JAMA*, vol. 316, no. 22, p. 2402, 2016.

[14] M.Sankar, K.Batri, and R.Parvathi, *Earliest diabetic retinopathy classification using deep convolution neural networks.pdf*, 2016.

[15] H. Pratt, F. Coenen, D. M. Broadbent, S. P. Harding, and Y. Zheng, "Convolutional neural networks for diabetic retinopathy," *Procedia Computer Science*, vol. 90, no. nil, pp. 200–205, 2016.

[16] G. Lim, M. L. Lee, W. Hsu, and T. Y. Wong, *Transformed representations for convolutional neural networks in diabetic retinopathy screening*, 2014.

[17] N. Petrick, H.-P. Chan, B. Sahiner, and D. Wei, "An adaptive density-weighted contrast enhancement filter for mammographic breast mass detection," *IEEE Transactions on Medical Imaging*, vol. 15, no. 1, pp. 59–67, 1996.

[18] F. C. Ghesu, B. Georgescu, Y. Zheng, J. Hornegger, and D. Comaniciu, "Marginal space deep learning: Efficient architecture for detection in volumetric image data," in *Medical Image Computing and Computer-Assisted Intervention – MICCAI 2015: 18th International Conference, Munich, Germany, October 5-9, 2015, Proceedings, Part I*, N. Navab, J. Hornegger, W. M. Wells, and A. F. Frangi, Eds. Cham: Springer International Publishing, 2015, pp. 710–718, ISBN: 978-3-319-24553-9.

[19] T. Brosch, Y. Yoo, L. Y. W. Tang, D. K. B. Li, A. Traboulsee, and R. Tam, "Deep convolutional encoder networks for multiple sclerosis lesion segmentation," in *Medical Image Computing and Computer-Assisted Intervention – MICCAI 2015: 18th International Conference, Munich, Germany, October 5-9, 2015, Proceedings, Part III*, N. Navab, J. Hornegger, W. M. Wells, and A. F. Frangi, Eds. Cham: Springer International Publishing, 2015, pp. 3–11, ISBN: 978-3-319-24574-4.

[20] M. J. J. P. van Grinsven, B. van Ginneken, C. B. Hoyng, T. Theelen, and C. I. Sánchez, "Fast convolutional neural network training using selective data sampling: Application to hemorrhage detection in color fundus images," *IEEE Transactions on Medical Imaging*, vol. 35, no. 5, pp. 1273–1284, 2016.

[21] C. Bishop, *Pattern recognition and machine learning*. New York, NY: Springer, 2006, ISBN: 978-0-387-31073-2.

[22] F. Rosenblatt, "The perceptron: A probabilistic model for information storage and organization in the brain.," *Psychological Review*, vol. 65, no. 6, pp. 386–408, 1958.

[23] P. J. Werbos, "Beyond regression: New tools for prediction and analysis in the behavioral sciences," PhD thesis, Harvard University, 1974.

[24] *Definition of a neural network*, `http://uhaweb.hartford.edu/compsci/neural-networks-definition.html`, Accessed:2017.

[25] D. E. Rumelhart, G. E. Hinton, and R. J. Williams, "Learning representations by back-propagating errors," *Nature*, vol. 323, no. 6088, pp. 533–536, 1986.

[26] *Artificial neural network*, `https://en.wikipedia.org/wiki/Artificial_neural_network`, Accessed:2017, 2017.

[27] I. Goodfellow, Y. Bengio, and A. Courville, *Deep Learning*. MIT Press, 2016, `http://www.deeplearningbook.org`.

[28] K. Fukushima, "Neocognitron: A self-organizing neural network model for a mechanism of pattern recognition unaffected by shift in position," *Biological Cybernetics*, vol. 36, no. 4, pp. 193–202, 1980.

[29] Y. LeCun, B. Boser, J. S. Denker, D. Henderson, R. E. Howard, W. Hubbard, and L. D. Jackel, "Backpropagation applied to handwritten zip code recognition," *Neural Computation*, vol. 1, no. 4, pp. 541–551, 1989.

[30] Y. LeCun, Y. Bengio, and G. Hinton, "Deep learning," *Nature*, vol. 521, no. 7553, pp. 436–444, 2015.

[31] A. Deshpande, *A beginner's guide to understanding convolutional neural networks part 2*, url=https://adeshpande3.github.io/adeshpande3.github.io/A-Beginner's-Guide-To-Understanding-Convolutional-Neural-Networks-Part-2/, Accessed:2017.

[32] Y. LeCun, L. Bottou, Y. Bengio, and P. Haffner, "Gradient-based learning applied to document recognition," in *Intelligent Signal Processing*, IEEE Press, 2001, pp. 306–351.

[33] A. Krizhevsky, I. Sutskever, and G. E. Hinton, "Imagenet classification with deep convolutional neural networks," in *Advances in Neural Information Processing Systems*, p. 2012.

[34] C. Szegedy, V. Vanhoucke, S. Ioffe, J. Shlens, and Z. Wojna, "Rethinking the inception architecture for computer vision," *CoRR*, 1999. arXiv: 1512.00567 [cs.CV].

[35] J. Jin, A. Dundar, and E. Culurciello, "Flattened convolutional neural networks for feedforward acceleration," *CoRR*, 1999. arXiv: 1412.5474 [cs.NE].

[36] K. He, X. Zhang, S. Ren, and J. Sun, "Deep residual learning for image recognition," *CoRR*, 1999. arXiv: 1512.03385 [cs.CV].

[37] N. Srivastava, G. E. Hinton, A. Krizhevsky, I. Sutskever, and R. Salakhutdinov, "Dropout: A simple way to prevent neural networks from overfitting.," *Journal of Machine Learning Research*, vol. 15, no. 1, pp. 1929–1958, 2014.

[38] T. Fawcett, "An introduction to roc analysis," *Pattern Recognition Letters*, vol. 27, no. 8, pp. 861–874, 2006.

[39] M. Mahy, L. Van Eycken, and A. Oosterlinck, "Evaluation of uniform color spaces developed after the adoption of cielab and cieluv," *Color Research And Application*, vol. 19, no. 2, 1994.

[40] *Https://www.zeiss.com/spectroscopy/solutions-applications/color-measurement.html*. Carl Zeiss Spectroscopy GmbH.

[41] R. L. Thorndike, "Who belongs in the family?" *Psychometrika*, vol. 18, no. 4, pp. 267–276, 1953.

[42] "Deep image: Scaling up image recognition," *CoRR*, vol. abs/1501.02876, 2015, Withdrawn.

[43] B. Graham, "Fractional max-pooling," *CoRR*, vol. abs/1412.6071, 2014.

[44] A. L. Maas, A. Y. Hannun, and A. Y. Ng, "Rectifier nonlinearities improve neural network acoustic models," in *In ICML Workshop on Deep Learning for Audio, Speech and Language Processing*, 2013.

[45] B. Xu, N. Wang, T. Chen, and M. Li, "Empirical evaluation of rectified activations in convolutional network," *CoRR*, vol. abs/1505.00853, 2015.

[46] K. He, X. Zhang, S. Ren, and J. Sun, "Delving deep into rectifiers: Surpassing human-level performance on imagenet classification," *CoRR*, 1999. arXiv: 1502.01852 [cs.CV].

[47] A. Karpathy, G. Toderici, S. Shetty, T. Leung, R. Sukthankar, and L. Fei-Fei, "Large-scale video classification with convolutional neural networks," in *Proceedings of the 2014 IEEE Conference on Computer Vision and Pattern Recognition*, ser. CVPR

’14, Washington, DC, USA: IEEE Computer Society, 2014, pp. 1725–1732, ISBN: 978-1-4799-5118-5.